

1.1.9.032 Next Generation Lithium-Ion Batteries: Advanced Anodes R&D

1.1.9.032 Next Generation Anodes for Lithium-Ion Batteries: Silicon (ANL, LBNL, ORNL, SNL, NREL)

Jack Vaughey, Point-of-Contact

Argonne National Laboratory
9700 South Cass Avenue
Argonne, IL 60439
Phone: (630) 252-8885
E-mail: vaughey@anl.gov

Brian Cunningham, DOE-EERE-VTO Program Manager

Hybrid Electric Systems, Battery R&D
Phone: (202) 287-5686
E-mail: brian.cunningham@ee.doe.gov

Start Date: 10/1/2016

End Date: 09/30/2020

Project Funding (FY19): \$2710K

DOE share: \$2710K

Non-DOE share: \$0

Table of Contents

Project Introduction (page 2)

Objectives (page 3)

Approach (page 4)

1. Results: Silicon-based Electrodes

Silicon Utilization	(page 5)
Conductive Additives	(page 7)
Binder Properties	(page 9)
Slurry Properties	(page 14)
Binder Modifications	(page 17)
Silicon-Binder Interactions	(page 18)
Conclusions: Silicon-based Electrodes	(page 21)

2. Results: Silicon Surface Modifications

Functionality	(page 21)
Silicon Tin Amorphous Films	(page 25)
Carbon-Coated Silicon / Binder Interactions	(page 29)
Interfacial Zintl Phase Formation	(page 35)
Zintl Electrolyte Properties	(page 39)
Conclusions Silicon Surface Modifications	(page 40)

3. Results: SEI Stability

Soluble SEI Components	(page 41)
------------------------	-----------

SEI Component Synthesis	(page 46)
Cathode Interactions	(page 46)
LHCE Electrolytes	(page 48)
Conclusions: SEI Stability	(page 50)
4. Key Publications	(page 51)
5. References	(page 52)

Project Introduction

Silicon has received significant attention as an alternative to the graphitic carbon negative electrode presently used in lithium-ion batteries due to its much higher capacity and general availability. Compared to graphitic carbons, silicon has nearly an order of magnitude higher capacity (~3600 mAh/g silicon vs 372 mAh/g graphite), however, several problems that limit its utility in commercial cells have been identified including large crystallographic expansion upon lithiation (~320%), slow lithium diffusion, and high reactivity at various states of charge. Combined, these materials properties can result in active particle cracking (stress-strain), particle isolation, electrolyte reactivity, and electrode delamination issues. These chemical reactivity and volume changes are manifested in SEI stability and cycling efficiency issues for the cell. Keeping this in mind, the large number of studies focused on silicon-based electrodes is a testament to the opportunity it presents but also the size of the challenge and innovation it inspires on multiple fronts. BatPaC, a techno-economic program

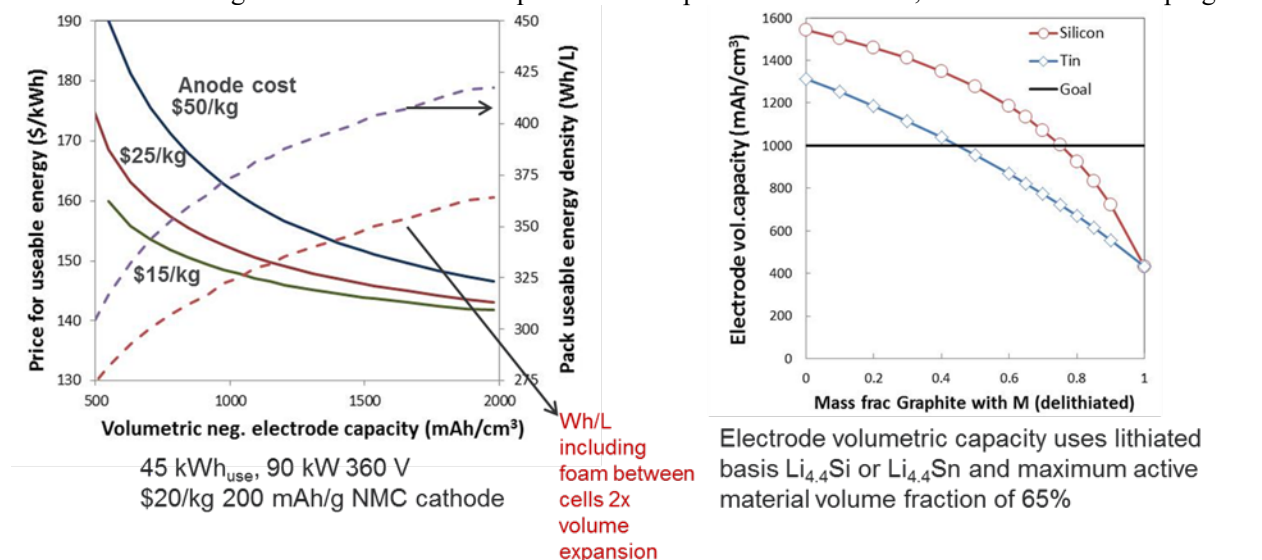


Figure 1.1.9.032.1. Battery Performance and Cost (BatPaC) model utilized to establish relevance by connecting pack to anode targets.

designed to model lithium-ion battery performance and cost, was utilized to establish program relevance by connecting DOE/USABC pack performance targets to anode targets. BatPac analysis of the needs for LIB anode science (see Figure 1.1.9.032.1, left frame) indicated that anode volumetric capacities greater than 1000 mAh/cm³ generally minimizes battery cost when coupled to an advanced NMC cathode. Note that higher capacities result in diminishing savings in cost. The analysis (right frame) also predicts that silicon-graphite electrodes with less than 75 wt% graphite can achieve the 1000 mAh/cm³ target.

Next Generation Anodes for Lithium-Ion Batteries, also referred to as the Silicon DeepDive Program, is a consortium of five National Laboratories assembled to tackle the barriers associated with development of an advanced lithium-ion negative electrode based upon silicon as the active material. This research program has several goals including establishing baseline silicon materials for research consistency obtained in quantities

sufficient for electrode preparation by the consortiums combined facilities and executing full cell development strategies that leverage DOE-EERE-VTO investments in electroactive materials and characterization. The primary objective of this program is to understand and eliminate the barriers to implementation of a silicon-based anode in a lithium-ion cell. The five National Laboratories involved are focused on a single program with continuous interaction, established protocols for analysis, and targets for developing both an understanding and a cell chemistry associated with advance negative electrodes for lithium-ion cells. This undertaking is a full electrode/full cell chemistry project leveraging common baseline electrodes prepared at the consortium facilities. All efforts are directed to understanding and developing the chemistry needed for advancing silicon-based anodes operating in full cells. Materials development efforts include active material development, binder synthesis, coatings, safety, and electrolyte additives. Efforts include diagnostic research from all partners, which span a wide range of electrochemical, chemical and structural characterization of the system across length- and time-scales. Specialized characterization techniques developed with DOE-EERE-VTO funding, include neutron diffraction studies, MAS-NMR and optical spectroscopy methods, and X-ray based techniques being employed to understand operation and failure mechanisms in silicon-based anodes. The project is managed as a single team effort spanning the Labs, with consensus decisions driving research directions and toward development of high-energy density lithium-ion batteries. A detailed list of participants is given in Figure 1.1.9.032.2.

CONTRIBUTORS AND ACKNOWLEDGMENT

Research Facilities		<ul style="list-style-type: none"> ▪ Cell Analysis, Modeling, and Prototyping (CAMP) ▪ Battery Manufacturing Facility (BMF) ▪ Battery Abuse Testing Laboratory (BATLab) 	
<ul style="list-style-type: none"> ▪ Post-Test Facility (PTF) ▪ Materials Engineering Research Facility (MERF) 			

Contributors			
<ul style="list-style-type: none"> ▪ Daniel Abraham ▪ Ira Bloom ▪ Su Ahmed ▪ Nasim Azimi ▪ Beth Armstrong ▪ Chunmei Ban ▪ M. Katie Burdette ▪ Anthony Burrell ▪ Saida Cora ▪ Jaclyn Coyle ▪ Dennis Dees ▪ Fulya Dogan ▪ Wesley Dose ▪ Alison Dunlop 	<ul style="list-style-type: none"> ▪ Yeyoung Ha ▪ Binghong Han ▪ Sang-Don Han ▪ Andrew Jansen ▪ Sisi Jiang ▪ Haiping Jia ▪ Christopher Johnson ▪ Baris Key ▪ Joel Kirner ▪ Robert Kostecki ▪ Bob Jin Kwon ▪ Xiaolin Li ▪ Chen Liao ▪ Min Ling ▪ Michael Liu 	<ul style="list-style-type: none"> ▪ Gao Liu ▪ Wenquan Lu ▪ Maria Jose Piernas Muñoz ▪ Jagjit Nanda ▪ Nate Neale ▪ K. Nie ▪ Bryant Polzin ▪ Krzysztof Pupek ▪ Marco-Tulio F. Rodrigues ▪ Rose Ruther ▪ Niya Sa ▪ Yangping Sheng ▪ Seoung-Bum Son ▪ Caleb Stetson ▪ Wei Tong 	<ul style="list-style-type: none"> ▪ Stephen Trask ▪ Jack Vaughey ▪ Gabriel Veith ▪ Qingliu Wu ▪ Yimin Wu ▪ Kang Yao ▪ Ji-Guang Zhang ▪ Linghong Zhang ▪ Lu Zhang ▪ John Zhang ▪ Tianvue Zheng ▪ Ting Zhang

Support for this work from Battery R&D, Office of Vehicle Technologies, DOE-EERE, is gratefully acknowledged – Brian Cunningham, Steven Boyd, and David Howell



Figure 1.1.9.032.2. Program participants including Laboratories, research facilities, and individual contributors.

Objectives

- Understand and overcome the science and technology barriers to the use of silicon-based anodes in high-energy density lithium-ion batteries for transportation applications.
 - Stabilize the SEI
 - Stabilize the electrode structure
- Demonstrate functional prototype lithium-ion cell chemistries that include a silicon-containing anode which meet the DOE/USABC performance targets.

Approach

Oak Ridge National Laboratory (ORNL), National Renewable Energy Laboratory (NREL), Sandia National Laboratory (SNL), Lawrence Berkeley National Laboratory (LBNL), and Argonne National Laboratory (ANL) have teamed together to form an integrated program dedicated to identifying, developing an understanding, and proposing solutions to the problems associated with the commercialization of silicon as an active component of a lithium-ion electrochemical cell. Technical targets have been developed and regular communications have been established across the team. Throughout the program, there is a planned focus on understanding, insights into, and advancement of silicon-based materials, electrodes, and cells. Advancements will be verified based on life and performance of full cells. Toward that end, baseline silicon-based materials, electrodes, and cells have been adopted, along with uniform full cell testing protocols.

In examining improvements, changes to the baseline cell technology will be assessed regularly and will be updated to reflect advances, new suppliers, and treatments based on the data and assessments from team members. Studies of the present baseline systems have adopted a testing protocol from the literature that has worked well for lithium-ion cells with silicon containing anodes. The test starts with three slow (C/20) formation cycles, an HPPC cycle, and then the C/3 aging cycles. The test ends with another HPPC cycle and three slower (C/20) cycles. All constant current cycling is symmetric between charge and discharge rates. The tests are run at 30°C. If there is little or no aging in the first 100 cycles, the protocol can be repeated. This protocol effectively examines capacity, impedance, and aging effects in about a month's worth of testing. The present baseline silicon was developed and produced by Paraclete Energy (Chelsea, MI) and has been made available to all participants on demand. The silicon was purchased in bulk from Paraclete to minimize batch to batch issues and electrode fabrication was done using consistent materials, compositions, and conditions. The cathode is a commercial 532 NMC Cathode available from CAMP, and the baseline electrolyte is 1.2M LiPF₆ in a 3:7 ratio of EC/EMC by weight (Gen2) plus 10 wt% FEC. Scale-up of materials, incorporation of materials advancements into electrodes, prototype cells, characterization, safety evaluation, abuse tolerance and testing of cells, are part of a wide range of integrated studies supported by battery research facilities at the National Labs working closely with the program. These research facilities include the Battery Abuse Testing Laboratory (BATLab), the Battery Manufacturing Facility (BMF), the Cell Analysis, Modeling, and Prototyping (CAMP), and the Post-Test Facility (PTF).

The fundamental understanding developed as part of the silicon DeepDive is based on extensive electrochemical and analytical studies of the components, electrodes, and cells conducted by researchers in the program. This effort contains in-situ and ex-situ studies on full and specialty cells, including reference electrode cells. Overall, the diagnostic studies are intended to help establish structure-composition-property relationships, including lithium-rich surface compounds, bulk transport, and kinetic phenomena. Together they form the basis for accurately assessing component and electrode failure modes and sets a path for advancements. Supported by the diagnostic studies, materials development on silicon-based materials, electrodes, and cells has been focused on enhancement of interfacial stability, accommodation of volume changes on lithiation, improvements in overall performance and life. A key avenue of research for this goal is the development and testing of surface coatings and electrolyte additives designed to modify and stabilize the dynamic silicon-electrolyte interface. In this past year we have added more diagnostic techniques designed to probe the role of additives on the rigidity, porosity, and transport properties of the surface electrolyte interphase (SEI). Keeping with the goals of using

full cell for the DeepDive effort, efforts aimed at understanding the slurry properties, role of binder protonation, and viscosity continues as a multi-Lab pathway to improve the baseline electrodes.

Communication of programmatic progress to battery community is critical. This will generally be accomplished through publications, presentations, reports, and reviews. Further, the program is open to industrial participation and/or collaboration that does not limit program innovation or the free flow of information. Finally, the DeepDive is highly integrated with the SEISta program, a sister program focused on stabilization of the silicon SEI layer. Generally, SEISta is focused on the development and characterization of model systems, surface analysis, well-defined thin film electrodes, and interfacial silicate phases and phenomena.

1. Results: Silicon-based Electrodes

Silicon Utilization: The silicon electrode development effort continued a focus on high-silicon (graphite-free) electrode formulations that it began in FY18. Since volume expansion issues associated with charged silicon anodes are dependent on the cell voltage, a goal was to understand with a silicon composite electrode (rather than the just the element) the role silicon particle volume expansion and contraction play in electrode performance versus extent of lithiation by evaluating multiple voltage window cutoffs for the anode. Previous efforts by CAMP utilized lithiation to as low as 10 mV versus Li⁺/Li, with limited enhancement of cycle life. The initial focus was a performance comparison of electrodes designed with 50 mV and 100 mV lithiation cutoff potential using three batches of baseline silicon material sourced from Paraclete Energy. Sample one was a Si batch annealed in air at 400°C to remove surface silica defects using conditions optimized previously. Samples two and three were high-silicon content electrode compositions noted below:

71:10:19 wt.% (silicon: conductive additive: LiPAA binder)

80:10:10 wt.% (silicon: conductive additive: LiPAA binder)

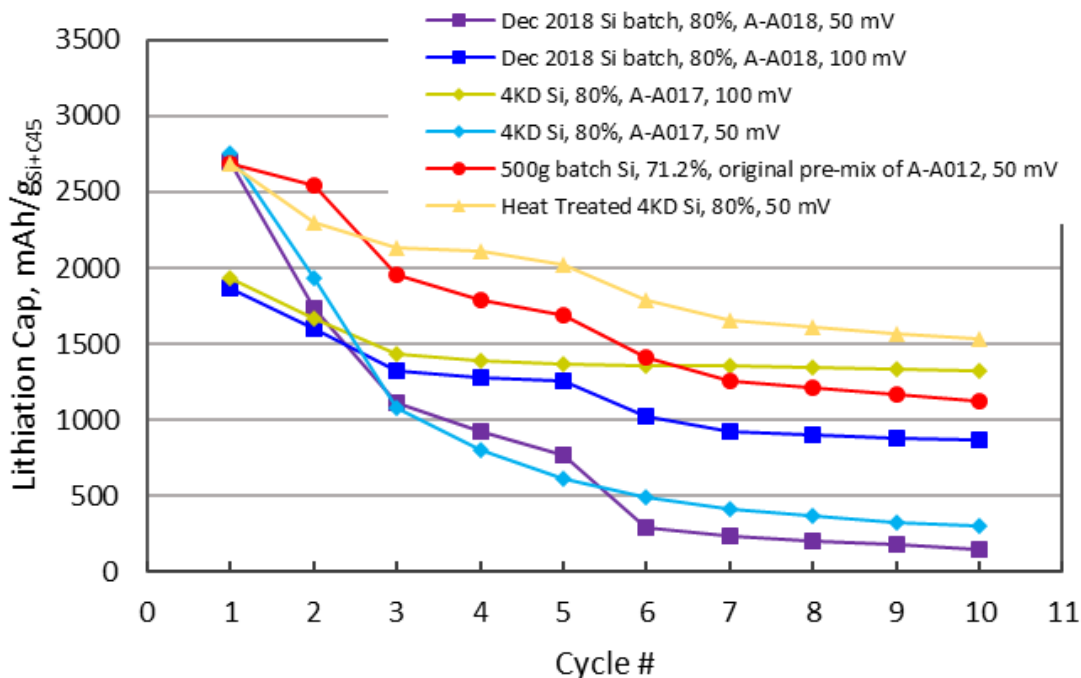


Figure 1.1.9.032.3. Lithiation capacity versus lithium metal for various graphite-free silicon electrodes fabricated by the CAMP Facility. These cells were cycled between 0.05 to 1.5 V or 0.1 to 1.5 V vs. Li⁺/Li as noted in the legend.

The half-cell performance of these cells is shown in Figure 1.1.9.032.3. From this plot it is noted that the capacity utilization and fade rate vary significantly between electrodes, however it is clear is that the first lithiation

capacity is very consistent for the electrode sets using a 50 mV and 100 mV cutoff potential. For samples that underwent the heat treatment in air at 400 °C, enhanced capacity utilization of the silicon compared to baseline was observed. This is consistent with previous reports although tradeoffs in lost active material, control of passivation thickness, and lithium silicate formation and dissolution have been noted in the DeepDive and SEISta programs.

Figure 1.1.9.032.4 is a comparison of full cell performance of the 15 wt. % silicon-graphite and a high-silicon graphite-free anodes versus a baseline NMC532 cathode baseline with the 50mV cutoff. The Si electrodes were matched to the NMC532 capacity loading that were included in this full cell study. This included the original baseline Si (electrodes: 15 wt.%) from NanoAmor (50-70 nm) from electrodes in the CAMP library at the correct loading. It is evident that both data sets have a similar but excessive capacity fade rate, regardless of the amount or source of silicon. The performance of the various sources of Si at 15 wt.% is exceptionally similar. For the 80 wt. % Si electrodes, the best capacity retention was seen for the 400°C air annealed Paraclete Si (black line) materials. While the same Si that was not heat treated resulted in a lower capacity, the capacity fade rate was similar for all Si electrodes.

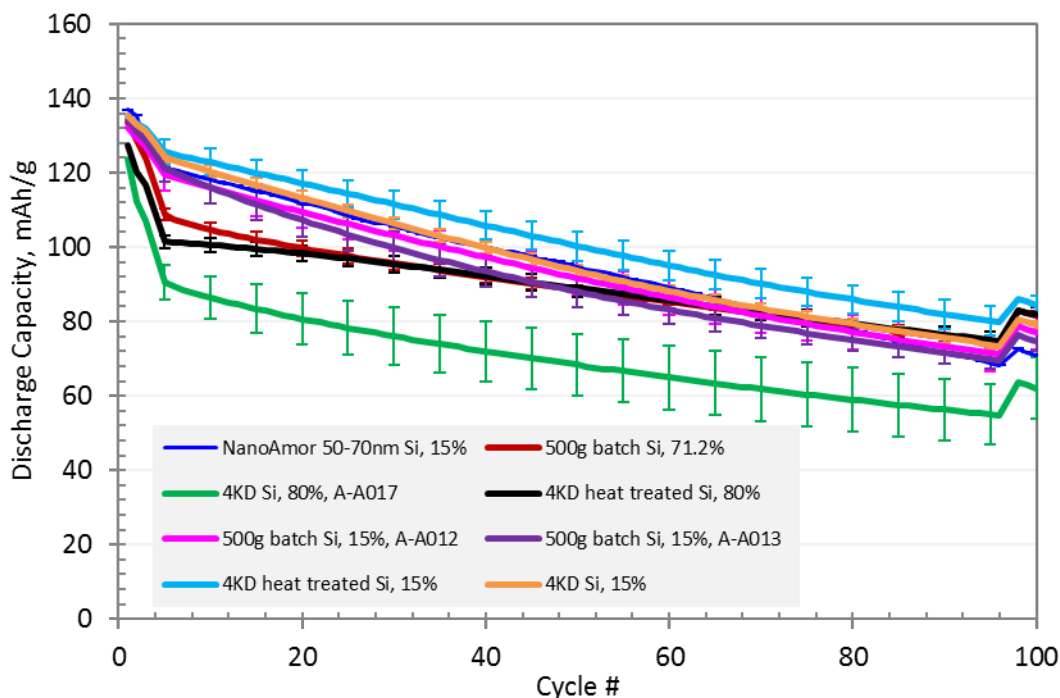


Figure 1.1.9.032.4. Full cell results using the silicon DeepDive protocol for the high-silicon graphite-free anodes and 15 wt.% Si in graphite composite. All anodes were tested against a capacity-matched NMC532 cathode. The anode to cathode capacity pairing for the electrode couples was based on the anode capacities achieved upon a 50-mV lithiation cutoff.

Comparing the half-cell and full-cell results, a portion of which was presented in **Figure 1.1.9.032.4**, we believe that the difference in capacity utilization and fade rate for the high-silicon electrodes is most likely due to subtle uncontrolled variations in mixing and coating of the slurries used to create the electrodes. These subtle variations are magnified greatly due to the high capacity of silicon, which is ten times the capacity of graphite. Such an effect would be expected with the relatively lower amounts of conductive additive used in these high-silicon electrodes. Supported by microscopy studies by ANL Post Test and ORNL teams, it is possible that the silicon particles are more easily isolated and electronically disconnect (partially or completely) from the electronic matrix of the electrode during cycling. These observations have led to joint efforts between ANL and ORNL to develop slurries that lead to more homogeneous electrodes with higher amounts of conductive additive and silicon content in the 50 – 70 wt.% range. Additional and related work in conjunction with the binder

development group (Lu Zhang/ANL) has been addressing the role of slurry viscosity, pH, and adhesion to the active silicon particles as a path to strengthening the physical properties of electrodes. For these tests, the silicon sources were from Paraclete Energy, the programmatic baseline material, to ensure surface chemistries are consistent.

Conductive Additives: Using Raman Spectroscopy mapping techniques, electrode homogeneity was explored and is presented in **Figure 1.1.9.032.5**. The *K-means clustering* algorithm was used to analyze the Raman mapping of each sample. The purpose of using K-means analysis is to partition the large set of the Raman spectra into a small groups or clusters of spectra that have similarities. Each spectrum in a frame of Raman mapping was categorized into three clusters, with each cluster color coded in **Figure 1.1.9.032.5**. The electrode is not uniform on a microscopic level. The blue region in the Raman map corresponds to a silicon rich, carbon black deficient region. The red region corresponds to a carbon black rich, silicon deficient region. The green region is the silicon/carbon black interface. As constructed the electrodes are best described as islands of carbon black dispersed in a sea of silicon. Because silicon has low intrinsic conductivity, contact between the carbon black and the majority of the silicon needs to be high to achieve the highest capacity on cycling. Inhomogeneities in the electrode structure due to particle size

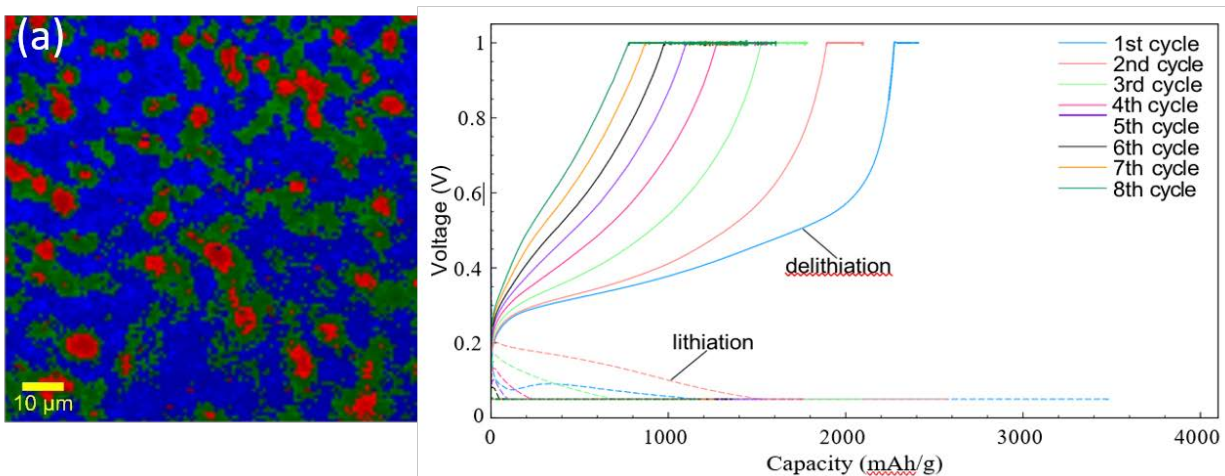


Figure 1.1.9.032.5. (Left) Raman mapping of pristine electrode. (Right) - cycling data for the electrodes

differences, surface chemistry, incomplete polymer interactions, and processing issues may exist. This inhomogeneity may translate to poor cycling performances depending on their defect concentrations and local changes in electrode structure (**Figure 1.1.9.032.5** right) that build-up on cycling.

Based on these electrode formulation observations, a study of various types of carbon that can be used to improve electrode stability and the electronic conductivity of the electrode matrix was performed with a high-silicon content (60 wt%). Increasing the concentration of conductive additive in these high-silicon electrodes should ensure that the silicon particles are more firmly connected to the electrode's electronic matrix during cycling. Based on small scale tests and discussions, two series of electrodes were created for the CAMP electrode library, one with 23 wt% electrochemically active Timcal SFG-6-L flake graphitic carbon, 60 wt.% Paraclete Si, 2 wt.% C45 carbon additive, and 15 wt.% LiPAA binder; the second uses a Kureha hard carbon instead of the graphitic carbon. These electrodes were designed to operate with a 100 mV lithiation cutoff (vs. Li^+/Li) as discussed previously.

With these different electrode slurries, electrodes required optimization of the coating wet gap, temperature zone profile, ventilation flow, and coating line speed. This was especially so for the SFG-6-L flakey graphite, as can be seen in **Figure 1.1.9.032.6** for various wet gap settings. The final specifications for both of these trial electrodes are summarized in **Figure 1.1.9.032.7**.

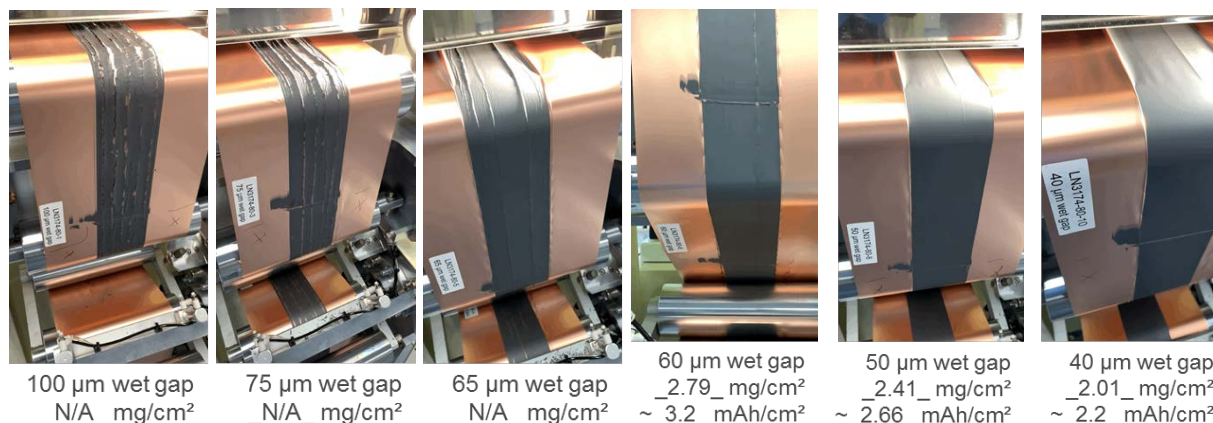


Figure 1.1.9.032.6. Variations in coating quality as a function of wet gap setting for 23 wt.% SFG-6-L flakey graphite with 60 wt.% silicon.

The half-cell performance of these two electrodes with 60 wt.% Si are shown in **Figure 1.1.9.032.8** with a comparison to two 80 wt.% Paraclete Si electrodes that are graphite-free (A-A017 “4 Kd Si” and A-A018 “Dec 2018 Si”; 10wt.% C45 and 10 wt.% LiPAA). Analysis of the data indicates that the Coulombic efficiency is significantly improved for the electrode with SFG-6-L flakey graphite compared to the 80 wt.% Si electrodes.

Anode: LN3174-80-10

60 wt% Paraclete Energy nSiO "G18-031-MM"
 23 wt% Timcal SFG-6-L flake graphite
 2 wt% Timcal C45 carbon
 15 wt% LiPAA (H₂O), LiOH titrated
Paraclete nSiO [G18-031-MM], "SS" = single sided -> Calendered by hand
 Cu Foil: 10 microns
 Total Electrode Thickness: 28 μm (SS)
 Coating Thickness: 18 μm (SS)
 Porosity: 44.4 %
 Total SS Coating Loading: 2.01 mg/cm²
 Total SS Coating Density: 1.12 g/cm³

Made by CAMP Facility

Anode: LN3174-81-8

60 wt% Paraclete Energy nSiO "G18-031-MM"
 23 wt% Kureha Hard Carbon
 2 wt% Timcal C45 carbon
 15 wt% LiPAA (H₂O), LiOH titrated
Paraclete nSiO [G18-031-MM], Kureha Carbotron P S(F) grade hard carbon Lot#: 220801, "SS" = single sided -> Calendered by hand
 Cu Foil: 10 microns
 Total Electrode Thickness: 28 μm (SS)
 Coating Thickness: 18 μm (SS)
 Porosity: 49.0 %
 Total SS Coating Loading: 1.84 mg/cm²
 Total SS Coating Density: 1.02 g/cm³

Made by CAMP Facility

Figure 1.1.9.032.7. Final specification for the two trial electrodes produced in this quarter based on 23 wt.% electrochemically active carbon (SFG-6-L flakey graphite and hard carbon) with 60 wt.% silicon.

After the second cycle this Si-flake graphite electrode has a delithiation specific capacity similar to the electrodes with 80 wt.% Si. Notably, the electrode made with a Kureha hard carbons had noticeably poorer Coulombic efficiency and lower specific capacity than the electrode made with a graphitic carbon.

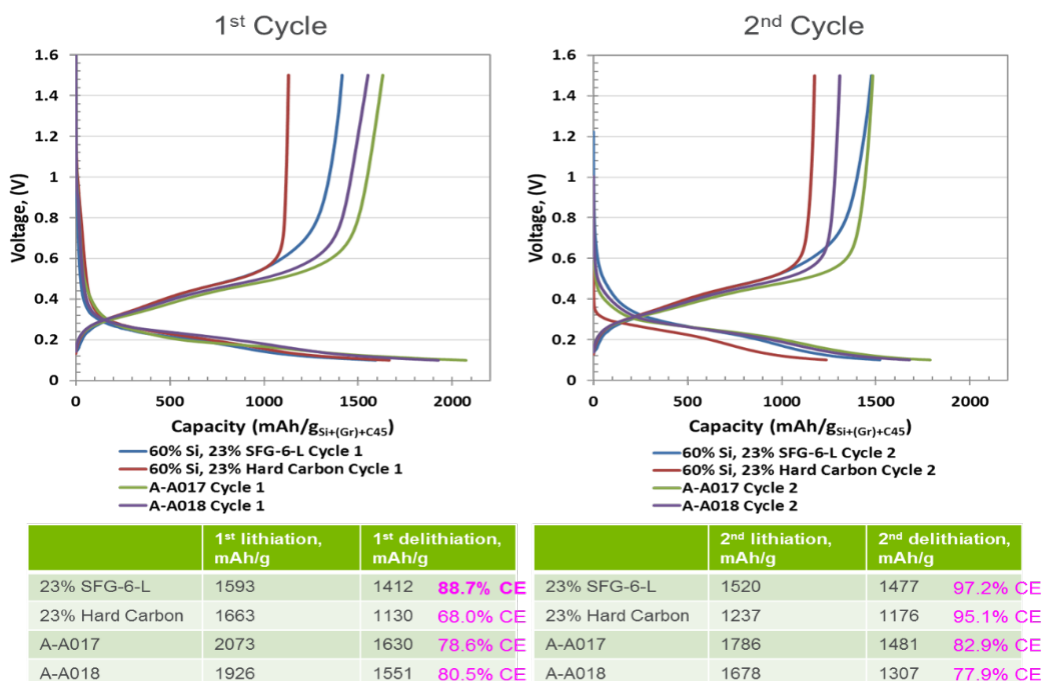


Figure 1.1.9.032.8. Lithiation & delithiation capacity versus lithium metal for 60 wt.% Si electrodes with 23 wt.% of either SFG-6-L flakey graphite or hard carbon. Comparison made to 80 wt.% graphite-free silicon electrodes (A-A017 “4 Kd Si” and A-A018 “Dec 2018 Si”; 10 wt.% C45 and 10 wt.% LiPAA), all fabricated by the CAMP Facility. These cells were cycled between 0.1 to 1.5 V vs. Li⁺/Li.

Binder Properties: To improve slurry properties, the use of PAA as a dispersant in the silicon electrode slurry was evaluated using several slurry modifications suggested by the Zeta-potential data from ORNL. Two slurries were tried with 1.8k PAA as the dispersant with either PAA as the binder, or LiPAA as the binder. Two more slurries were prepared without the dispersant to establish a baseline for this study. The PAA and LiPAA were 450k molecular weight. The compositions (dry wt. %) were as follows:

- i. 80 / 10 / 9.5 / 0.5 [Si/C-45/450k PAA binder/1.8k PAA dispersant, water based]
- ii. 80 / 10 / 10 [Si/C-45/450k PAA binder, water based]
- iii. 80 / 10 / 9.5 / 0.5 [Si/C-45/450k LiPAA binder/1.8k PAA dispersant, water based]
- iv. 80 / 10 / 10 [Si/C-45/450k LiPAA binder, water based]

Early data and discussions have highlighted that the order of addition is a variable that needs to be explored and will be a focus in FY20. The slurries above were mixed all at once in a planetary ball mill as a first trial. The rheology of the slurries was investigated and is shown in **Figure 1.1.9.032.9** for the slurries based on LiPAA as the binder, with and without the PAA dispersant. Overall, the viscosity-shear rate behavior was very similar, with the dispersant lowering the viscosity slightly, as can be expected.

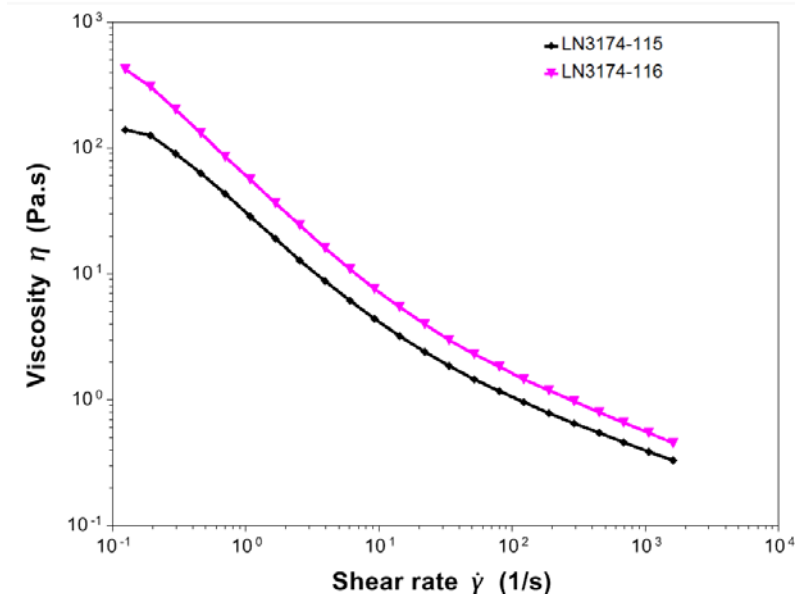


Figure 1.1.9.032.9. Viscosity vs. shear rate for 80 wt.% Si using LiPAA binder with PAA dispersant (LN3174-115) and without PAA dispersant (LN3174-116). Rheology measurement performed using a cone-plate geometry with a cone diameter of 20 mm and an angle of 2°. The temperature was held at 25 °C.

Initial baseline electrode studies based on LiPAA indicated they were much more uniform than the electrodes based on PAA binder. This was consistent with previously reported CAMP studies establishing the LiPAA-based electrodes as the baseline. While previous PAA-based slurries and electrodes showed inferior lamination properties, the addition of the dispersant to date has shown only small changes in electrode quality. However early state testing of multiple electrodes in a half cell configuration indicates that the cells with PAA as the binder have far better capacity utilization. For comparison the viscosity versus shear rate plot for an SFG6 graphitic carbon electrode with a LiPAA binder is shown in **Figure 1.1.9.032.10**.

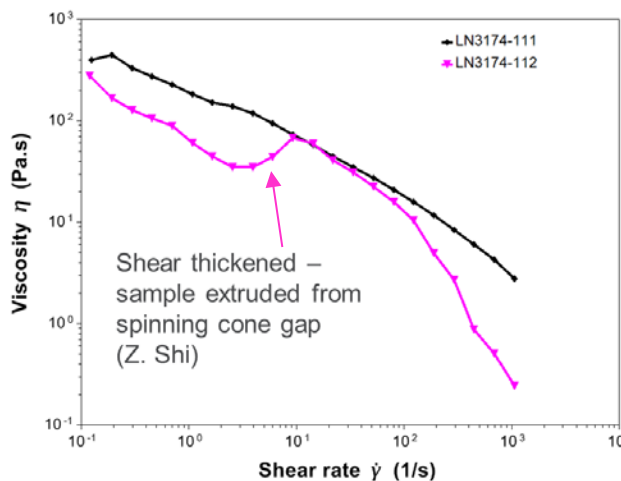


Figure 1.1.9.032.10. Viscosity vs. shear rate for a SFG-6L graphite electrode (no silicon) using LiPAA binder dispersant (black curve, LN3174-111), and for a SFG-6L graphite electrode (no silicon) with PAA binder (magenta curve, LN3174-112). Slurries consisted of 88 wt.% graphite, 2 wt.% C45 carbon, and 10 wt.% binder. Rheology measurement performed using a cone-plate geometry with a cone diameter of 20 mm and an angle of 2°. The temperature was held at 25 °C.

To better understand these observations, the solution properties of the slurries were investigated. The role of the binder, in addition to adhesion to particles and the current collector foil, additionally involves mediating

electrode formation and homogeneity which will influence SEI formation and electrode stability as the Si particles expand and contract. To address this interest, ultra-small angle neutron scattering (USANS) experiments on PAA solutions and PAA solutions with high concentrations of silicon with and without shear has been performed. These shear conditions reflect what occurs during electrode casting and slurry fabrication. USANS is an elastic neutron scattering method where incident neutrons are scattered at very small angles to measure large macrostructural organizations in solids, liquids and mixtures (100-3000 nm). USANS is particularly sensitive to hydrogen containing molecules (PAA) but insensitive to Si. As a result, the data fit provides insights to the polymer structure and dynamics.

For these experiments 450K MW PAA and silicon were obtained from the CAMP facility and used as received. The materials were dispersed in D₂O which allows significant contrast to observe the complex structure of the PAA. **Figure 1.1.9.032.11** shows the rheology data measured for the PAA solution and a PAA/Si/CB slurry used to fabricate electrodes at CAMP. The data for the PAA shows an initial flat (Newtonian) viscosity to about 20 Hz followed by a decrease in viscosity attributed to shear thinning due to changes in the PAA conformation within the suspension. In contrast, the slurry shows a more significant shear thinning processes followed by Newtonian behavior then a larger shear thinning behavior at shear rates greater than 20 Hz. This rheological response is indicative of complex interactions within the slurry and point to different polymer structures depending on shear rates which will influence electrode formation and could help explain the differences in performance reported in the literature for PAA-based electrodes.

The USANS data collected for the samples at 0 and 30 Hz are shown in **Figure 1.1.9.032.12**. The data is presented as intensity versus \AA^{-1} . USANS data was fit with the correlation length model described by Equation 1. The correlation length model characterizes polymer and colloidal solutions on multiple length scales from polymer chain packing to agglomeration. This allows for the exploration of the slurry system on a length scale from 200 nm to 10 microns. Q is a length scale measurement in reciprocal space. The first term represents the Porod scattering at low Q ranges, the second term characterizes the Lorentzian scattering at high Q ranges, and the third term, B is a background correction term. Porod-type scattering represents large features, such as polymer aggregation, while Lorentzian scattering represents small features, such as density of polymer chains in a polymer cluster.

$$(1) \quad I(Q) = A/Q^n + C/(1 + (QL)^m) + B$$

The exponent n characterizes the shape of the particles or aggregates as surface fractals, while the exponent m represents the density of polymer chain packing. The scaling factor A has an inverse relationship with the amount of polymer agglomeration on a micron length scale, while the scaling factor C represents polymer aggregation on a 300 nm to 1-micron length scale. The final parameter L is correlation length which represents the size of a polymer cluster.

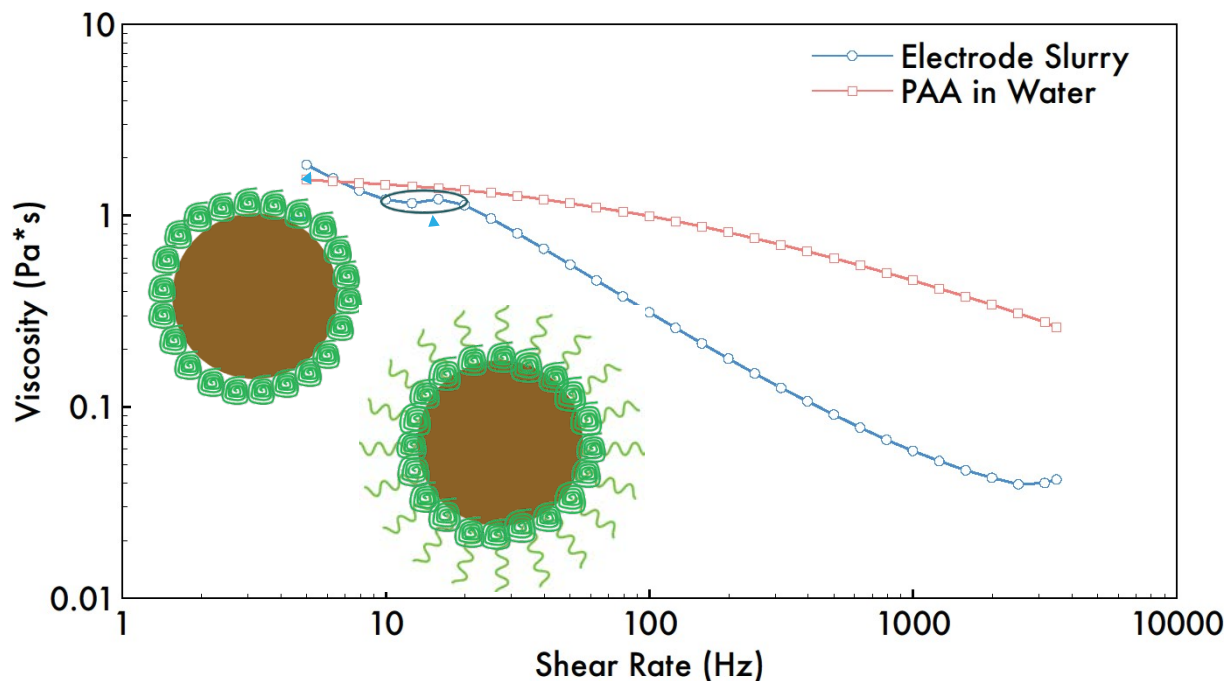


Figure 1.1.9.032.11. Viscosity versus shear rate curve for silicon electrode slurry. Inset schematic from left to right depict 1) extremely collapsed polymer chains on a silicon particle, 2) a mixture of extremely collapsed polymer chains and extended polymer chains as well as polymer that has been sheared and is now in the water phase, and 3) silicon particle aggregation at high shear rates. The line is added to guide the eye.

Based on our previous experience, a binder needs to exist as a polymer ellipsoid ($n=2-3$) where the ellipsoid can interact with other polymer chains forming a polymer network homogeneously distributed throughout the electrode slurry with and without shear. Additionally, agglomeration ($1-10\ \mu\text{m}$ length scale) and aggregation ($0.3-1\ \mu\text{m}$ length scale) of the polymers tend to mediate electrode homogeneity and dispersion. Fitting the PAA data revealed that PAA agglomerates and aggregates at shear rates less than approximately 50 Hz. (The agglomeration parameter, A , decreases from 8.9 to 4×10^{-4} , and the aggregation parameter, C , increases from 2.1×10^9 and 9.1×10^9 .) This is typical behavior in polymer solutions as the polymer becomes entangled with itself causing an increase in agglomeration. At a certain shear rate, the shear stress overcomes the critical entanglement parameter of the polymer and the polymer shear thins. Shear thinning occurs when polymer-polymer interactions are broken by the shear force. The polymer chains then align in the direction of shear and the polymer-polymer interactions are not reformed until shear is removed. The observed changes in the PAA data are consistent with the rheology data in **Figure 1.1.9.032.11** showing shear thinning behavior and is due to these changes in the PAA in solution.

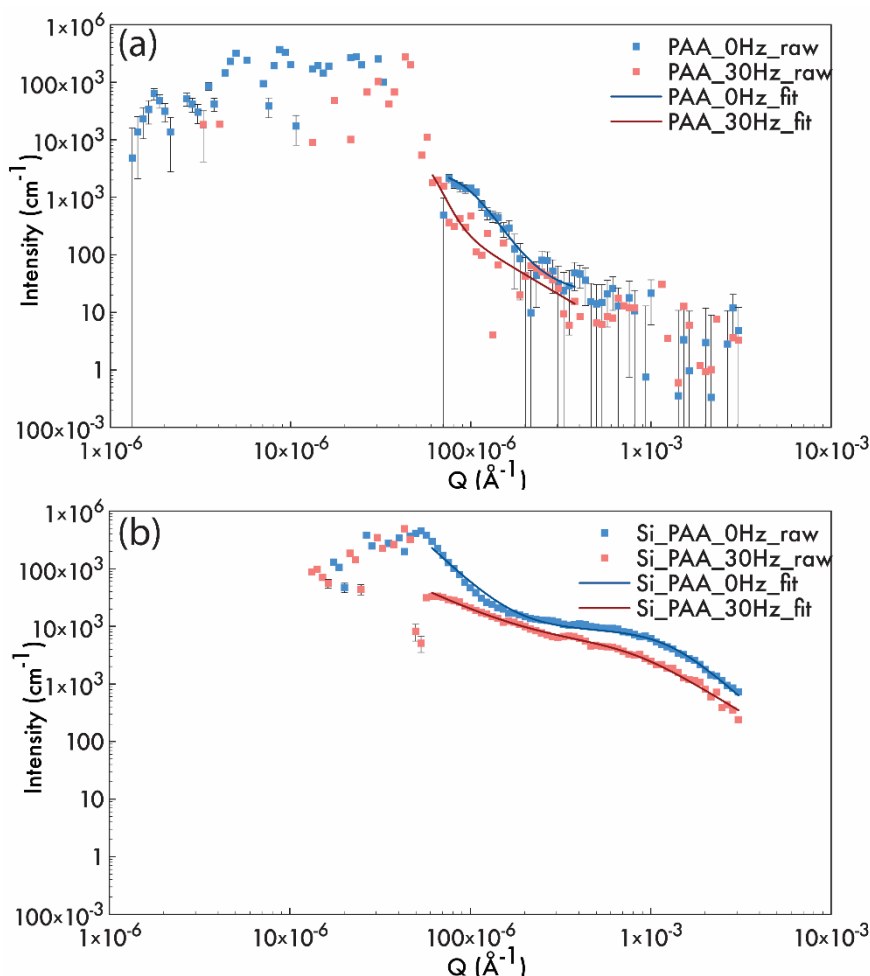


Figure 1.1.9.032.12. Intensity versus Q ultra small angle neutron scattering plots of (a) 14 wt% solution of 450,000 g/mol poly(acrylic acid) in deuterated water at 0 Hz and 30 Hz and (b) a 10 wt% solution of 450,000 g/mol poly(acrylic acid) and silicon nanoparticles (17 wt%) in deuterated water at 0 Hz (experimental data=blue circles, fitted data=blue lines) and 30 Hz (experimental data=red circles, fitted data=red lines).

The addition of silicon results in major changes in the solution polymer structure. Agglomeration and aggregation decrease upon an increase in shear rate with the introduction of silicon. This is the opposite of what was observed with the PAA alone. This may be a result of several possibilities including: 1) PAA chains interactions strongly adsorb to the silicon surface results but the polymer chains elongate and disentangle, 2) PAA desorbs from silicon anode upon shear and disentangle from one other, and 3) extra PAA that cannot adsorb to silicon creates lubrication layers which do not allow PAA chains adhered to other silicon particles to interact with one another. Analysis of USANS data shows that the PAA chains in the Si/PAA slurry are elongating as the L parameter increases from 76 nm to 120 nm upon shear. Elongation implies that polymer chains are disentangling from one another and polymer-polymer interactions are broken. Elongation and disentanglement of the polymer chains are supported by analysis of n parameter where the aggregate goes from a hard sphere ($n=4$) to a polymer ellipsoid ($n=2.6$) as shear rate is increased. For a polymer to exhibit crystal-like scattering ($n=4$), the polymer chain must be highly collapsed and have almost no free volume. For this same polymer to morph into a polymer ellipsoid upon shear, the polymer chains must elongate and begin to fold back on themselves and one another. This data is consistent with the rheology data and demonstrates that the origin of

the shear thinning is a slight elongation of the bound polymers. A schematic of this Si/PAA architecture is shown in **Figure 1.1.9.032.11**.

The data analysis reveals some surprising differences between the pure PAA and Si/PAA mixture. The PAA solution is comprised of large PAA clusters well dispersed in solution (~1000 nm). The addition of the Si particles causes PAA condensation forming ~76 nm particles, a nearly 10-fold decrease in size due to association with the silicon materials. These bound PAA molecules are strongly associated and not well dispersed in solution. This would indicate the PAA is acting to stabilize the Si in suspension but not interacting to form an extended network which we hypothesize is needed to form a stable electrode.

The properties of the polymeric binder are derived not only from the shear properties and molecular weight, but also the relative pH, functional groups, and viscosity. For baseline electrodes, LiPAA-based binders were chosen based on experimental evidence of final electrode structure. This was believed to be derived from superior viscosity properties associated with slurries with high lithiation. This advantage of better initial electrodes was in part offset by slightly better performance for cells derived from electrodes that were created using an approximately pH neutral PAA binder system. The higher pH used for the heavily lithiated PAA binder systems adversely affects chemical stability of Si particles in the slurry (dissolution of SiO₂), binding strength of PAA, and cycling performance of the silicon anodes due to the involvement of strong base of LiOH. Currently, only *N*-methyl-2-pyrrolidone (NMP) and water have been widely used as processing solvent for silicon electrodes, and the fabricated cells behave drastically differently. Despite the drastic impacts, the role of the processing solvents is not clear.

With these observations, we have investigated alternative methods to generate a more basic solution pH but at lower lithium cation contents to improve the viscosities and processing of the baseline PAA-based slurries. Initially, ammonia (NH₃) and triethylamine (Et₃N) were used as alternative neutralizing reagent to improve the rheological properties of PAA solutions. These additives were in part chosen because after the advantages associated with processing at a more neutral pH were built into the electrode, gentle heating would remove the additives from the electrode in a clean one-step process. A series of SAXS (Small Angle X-ray Scattering) experiments were used to understand the solvation behavior of PAA in various solvents as it related to the basic additives, processed into Si content electrodes and evaluated in Li half cells. These experiments are complimentary to the neutron diffraction studies noted earlier.

Slurry Properties: According to our previous study, aqueous PAA-Li solutions have higher viscosity at low shear rate and better shear thinning at high shear rate than pristine PAA solution. Therefore, more water should be needed for PAA-Li slurry to achieve the desired fluidity. For example, PAA-85% Li slurry requires three times of water to reach the ideal state for lamination compared to that of pristine PAA slurry. The resulting PAA-85% Li slurry is thus more dilute with better dispersion of electrode materials, and less effected by the water

evaporation, which is observed all the time in dry rooms. However, PAA-Li binders can lead to more degradation of the fabricated electrodes, which we believe is caused by the increased pH value of the binder solution and weaker binding strength provided by lithiated binder. To address this issue, ammonia (NH_3) and triethylamine

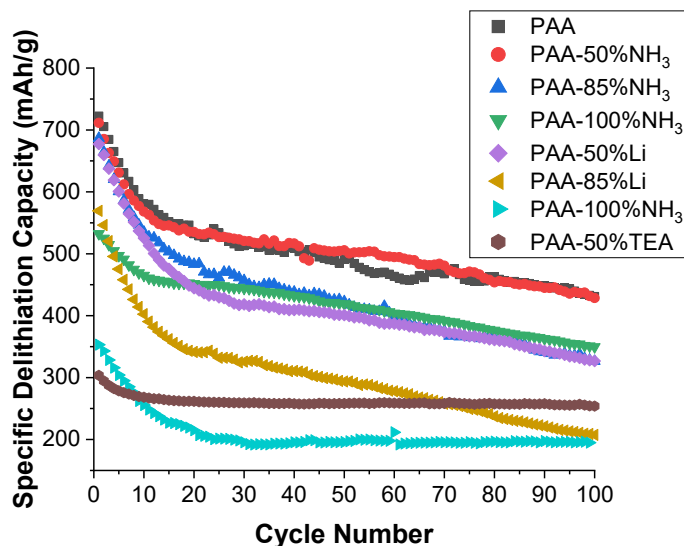


Figure 1.1.9.032.14. Specific delithiation capacity profiles of Li half cells using electrodes containing 73 wt% graphite, 15 wt% Si, 10 wt% modified PAA binders, and 2 wt% C45 over 100 cycles at C/3 rate.

(Et_3N , TEA) were utilized as neutralizing reagent instead of LiOH. These weak bases can modify the viscosity of the PAA solution in a similar way as LiOH does but with less of an increase of pH value. As shown in **Figure 1.1.9.032.13** the viscosity and shear thinning of PAA solutions neutralized by NH_3 (i.e., PAA- NH_3) is comparable with the current standard PAA-Li binder used by CAMP (i.e., PAA-85%Li with pH of 6). The pH value of PAA- NH_3 solutions (e.g., pH of PAA-85% NH_3 = 5) is lower than that of PAA-85%Li solution. PAA solutions modified by Et_3N (i.e., PAA-TEA) showed even more viscosity improvements due to the bulky $[\text{Et}_3\text{NH}]^+$ cations. For example, PAA-TEA solution with only 50% of Et_3N achieved similar viscosity and shear thinning as PAA-85%Li solution. The pH of PAA-TEA solutions is even lower (e.g., pH of PAA-50% TEA = 4.5). In addition, these weak bases could be removed from the electrode by thermal decomposition during the drying process at high temperature in vacuo. IR analysis for PAA- NH_3 binders after thermal treatment showed a distinct peak around 1700 cm^{-1} , indicating the existence of pristine PAA. Therefore, the binding strength of PAA binder could be restored since the ammonium carboxylate groups will convert to carboxylic acid groups after thermal decomposition. The capacity profiles of graphite-Si composite electrodes fabricated using these modified PAA binders were summarized in **Figure 1.1.9.032.14**. The cells were subjected to three formation cycles between 0.01 V and 1.50 V at C/20 rate, followed by 100 aging cycles at C/3 rate. PAA-50%TEA cells have much lower initial capacity (303 mAh/g) than pristine PAA cells (722 mAh/g). By looking into the differential capacity profile of a PAA-50% TEA cell, most of the capacity resulting from Si was lost during formation cycles, possibly due to the increased impedance by the large $[\text{Et}_3\text{NH}]^+$ cations. On the other hand, PAA- NH_3 cells have higher initial capacity, higher average capacity, and better capacity retention than those of PAA-Li cells. For example, PAA-85% NH_3 cells have initial capacity of 686 mAh/g, average capacity of 492 mAh/g while PAA-85%Li cells have initial capacity of 569 mAh/g and average capacity of 303 mAh/g. Interestingly, PAA-100% NH_3 cells have slightly lower capacity than PAA-85% NH_3 cells during the first 50 cycles, then the performance catches up and becomes pretty much identical. PAA-100%Li cell has the worst performance among the tested cells as expected due to the aforementioned reasons. Overall, PAA-50% NH_3 solution seems to achieve a good balance with significantly improved rheological properties and comparable performance as pristine PAA cells. We feel confident this new binder neutralization approach is superior to the lithiation approach.

Small-angle X-ray scattering (SAXS) analysis was utilized to investigate the solvation behavior of PAA binders at the APS facility at Argonne by beamline scientist Tao Li (**Figure 1.1.9.032.15**). SAXS can detect the density difference in a sample at nanoscales and therefore determine size, and shape information of the polymers. The radius of gyration (R_g) is a key parameter that is related to the particle sizes and can be obtained from SAXS signals by applying unified fit to the broad peak composed of a Guinier part and a power law tail in each profile. As shown in **Figure 1.1.9.032.15**, the results showed that R_g values dropped significantly by adding bases to

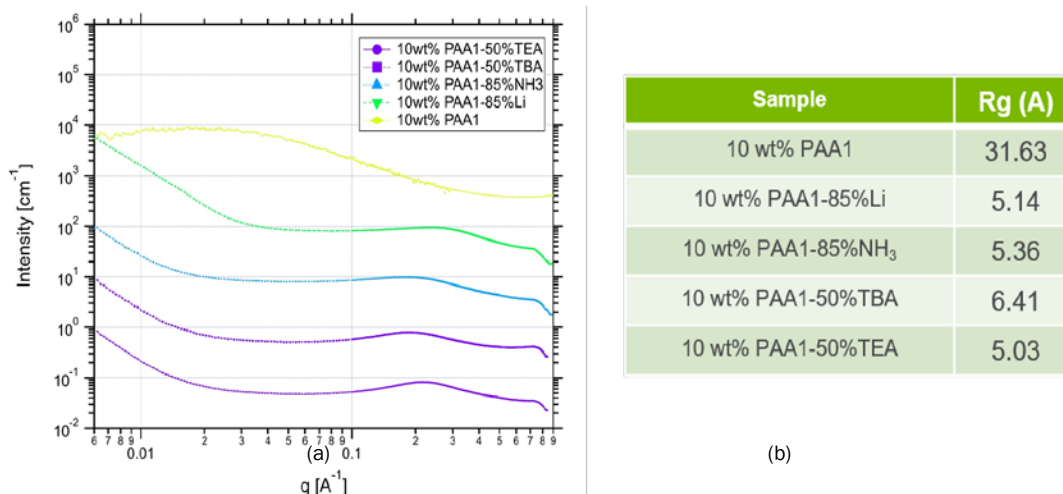


Figure 1.1.9.032.15. (a) Small angle X-Ray scattering (SAXS) profiles for binder solutions; (b) Sample information and R_g of the modified PAA solutions.

PAA solution. For a given volume, smaller R_g indicates that the shape of the particle is closer to sphere (i.e., smaller surface area for a given volume) and larger R_g is related to more stretched polymer conformations. Based on the results, we suspect that the better cycling performance of PAA binders, whose solution has a large R_g value (31.63), is maybe resulting from the stretched-out conformation that could prompt the interaction or adhesion with silicon particles. This may explain why the performance of PAA-NH₃ cells compared to PAA cell as the R_g values of PAA-NH₃ solution (5.36) is much smaller.

Moreover, as we observe drastic difference when NMP solvent was used to fabricated silicon electrodes, it is of crucial importance to understand why the changing of processing solvents impact the cycling performance. We adapted SAXs to probe this relationship. Several organic solvents or organic solvent/water mixtures were selected based on certain properties (e.g., boiling point, solubility of PAA, dielectric constant). By using similar testing protocols as shown above, the R_g values of PAA in these solvents as well as cycling performance of the corresponding cells were summarized in **Figure 1.1.9.032.16**. Right away, we notice the bigger R_g is still from PAA/ water solution and that is also the case in cycling performance. Electrodes fabricated using 1,4-dioxane (PAA-dioxane) and N,N-dimethylformamide (PAA-DMF) have similar initial capacity compared to electrodes fabricated using water (PAA-H₂O), but suffer more severe capacity loss during the first 20 cycles. Electrodes processed via N-methyl-2-pyrrolidone (PAA-NMP) and ethanol (PAA-EtOH) showed significantly lower initial capacity than PAA-H₂O electrodes. Since PAA-H₂O electrodes outperformed all the tested electrodes fabricated using organic processing solvents, organic solvent/water mixtures were prepared to study

the role of water. For example, electrodes fabricated using equal weight mixture of 1,4-dioxane and water (PAA-dioxane/H₂O) showed improved performance than PAA-dioxane, but not as good as PAA-H₂O electrodes. The *R_g* of PAA in 1,4-dioxane/water mixture also falls in between that of pure water and 1,4-dioxane, which is consistent with our hypothesis relating *R_g* and cycling performance. The outstanding performance of water might be a combined result of solubility, pH, dielectric constant, evaporation rate, and is under investigation.

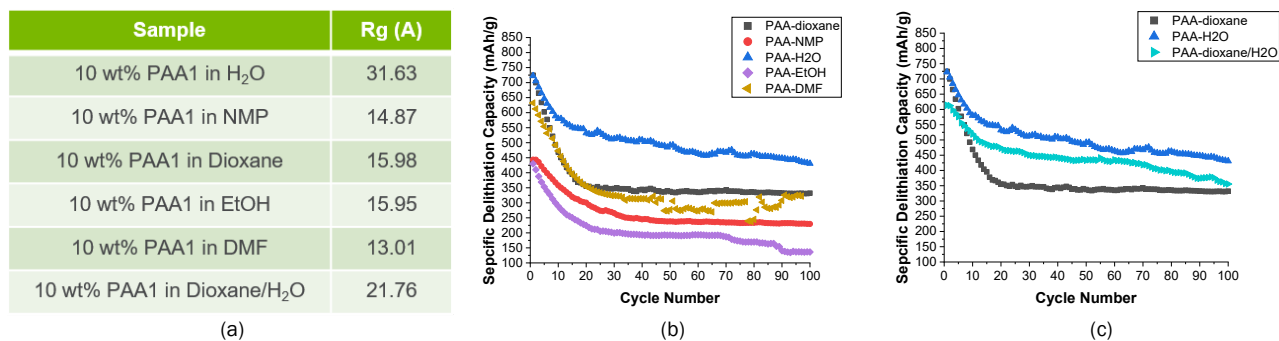


Figure 1.1.9.032.16 (a) Sample information and *R_g* of PAA solutions; (b) Specific delithiation capacity profiles of half cells using electrodes containing 73 wt% graphite, 15 wt% Si, 10 wt% PAA binders in organic processing solvent, and 2 wt% C45 over 100 cycles at C/3 rate; (c) Specific delithiation capacity profiles of half cells using electrodes containing 73 wt% graphite, 15 wt% Si, 10 wt% PAA binders in mixed processing solvent, and 2 wt% C45 over 100 cycles at C/3 rate.

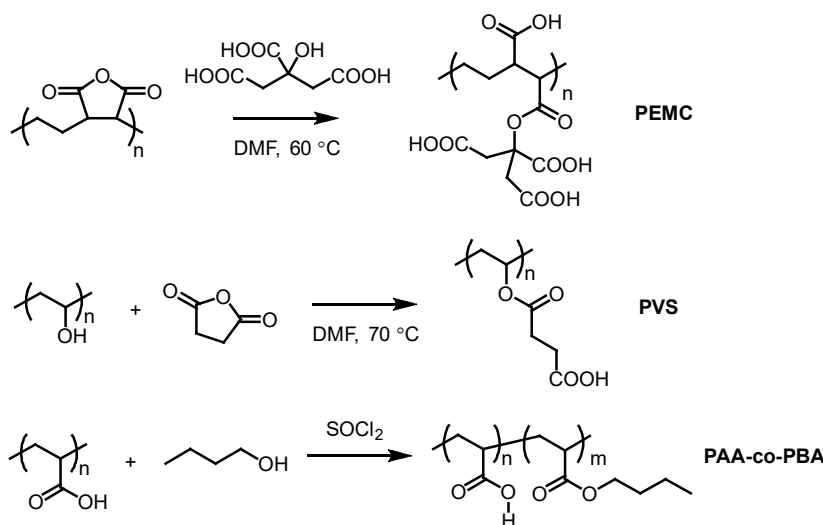


Figure 1.1.9.032.17. Synthetic scheme of PAA analogues with modified properties.

Binder Modifications: Based on these data, new modifications to the PAA system were suggested relating the structure-performance relationships of PAA-based binders. As a result several PAA analogues were designed and synthesized as new binder materials including poly(ethylene-alt-maleic acid monocitrate) (PEMC), poly(vinyl succinate) (PVS), and poly(acrylic acid-co-butyl acrylate) (PAA-co-PBA) (**Figure 1.1.9.032.17**). These polymers have modified properties compared to PAA, such as adhesion/cohesion (e.g., PEMC), hydrophilicity/hydrophobicity (e.g., PVS and PAA-co-PBA), and glass transition temperature (e.g., PAA-co-PBA). The purity of these synthesized polymers was confirmed by ¹H NMR analysis. The cycling tests of these new polymers as binders for Si electrode are ongoing.

Silicon-Binder Interactions: Using silicon nanomaterials is a widely accepted strategy for mitigating the volume expansion associated with the lithiation of silicon and the accompanying capacity fade. However, the high surface area of silicon nanomaterials provides more opportunity for electrolyte decomposition which leads to high irreversible capacity loss and low Coulombic efficiency. By using model crystalline electrodes, a more thorough understanding of the initial lithiation mechanics of the silicon crystalline particles is possible. This work is targeted at the initial crack formation of silicon and how the polymeric capping layers associated with binder interactions are affected by lithiation depth (state of charge) and cracking of the crystalline silicon.

Using thin film samples, the formation of buckled silicon within a thin film induced by the anisotropic lithiation of crystalline Si during the 1st lithiation along the $\langle 110 \rangle$ direction was identified. We also noted that as the delithiation proceeded, new cracks oriented along the $\langle 100 \rangle$ direction appear in the intact area where no *geological* deformation occurred during the previous lithiation (**Figure 1.1.9.032.18**). The $\langle 100 \rangle$ -oriented cracking followed the linear elastic mechanism developed for multilayer structures. Using a linear elastic fracture mechanic (LEFM) model, the results implied that the $\langle 100 \rangle$ -oriented cracking behavior depends on the mechanical properties of the Si substrate and the amorphous Li_xSi layer.

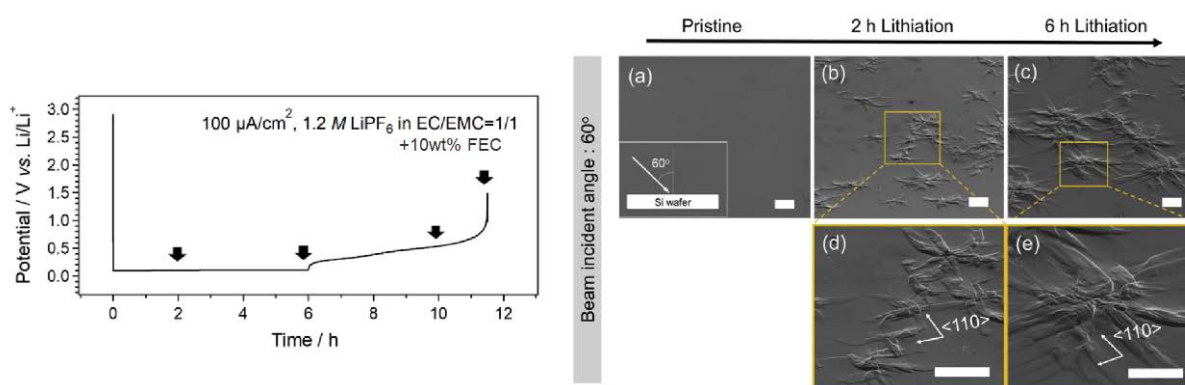


Figure 1.1.9.032.18. Electrochemically Induced Fracture Method. LEFT: Electrochemical cycling conditions used to induce fracturing, where arrows represent times where samples were analyzed via SEM. RIGHT: SEM data of sample in pristine state (a) and following (b,d) 2 h and (c,e) 6 h lithiation.

For these studies, the LEFM model assumes an elastic deformation and is known to fail at the *plastic* zone at the crack tip. For the LEFM model to be absolutely applicable, the plastic zone at crack tip must be small with respect to the crack length and dimensions of the sample. Thus, as the ratio of the crack length to the full sample thickness increases, more plastic deformation/types of fracture occur. **Figure 1.1.9.032.19** shows that the cracking behavior only follows LEFM-type mechanisms for thicknesses larger than 1 mm thickness. It has been noted that when 675 μm -thick samples are used, the failure mode also includes compression, slabbing, shearing, and microcracking behavior. In the context of the DeepDive effort, the silicon substrates used will be thin enough to exhibit the complex behavior that will be more analogous to the cracking dynamics observed in baseline silicon electrodes.

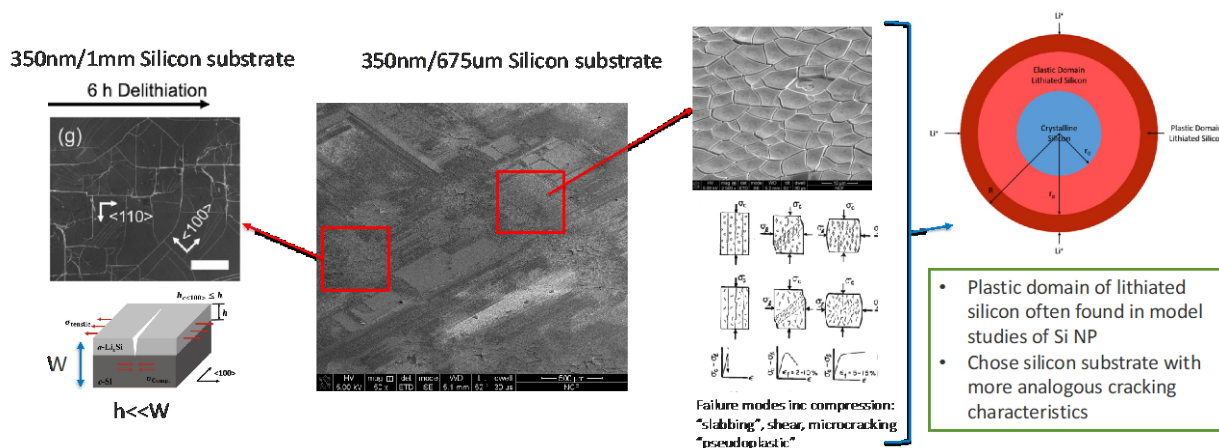


Figure 1.1.9.032.19. Limitations of the linear elastic fracture mechanics (LEFM) model based on the thickness of the silicon wafer. For thick wafers (1 mm), crack propagation occurs along crystallographic directions. For thinner wafers (675 μ m), LEFM mechanics cannot be applied. Rather, plastic deformation occurs resulting in a number of different failure modes including compression, slabbing, shear, microcracking, and pseudoplastic behavior—similar to the cracking behavior expected from silicon nanoparticles. SEM data and schematic on left from NREL.

With appropriate model silicon wafer thickness established, the mechanical properties of the top surface layer of the crystalline silicon substrates were modified by adding a polymeric capping layer, designed to mimic the properties of the binders used, and observed how these polymeric layers affect the electrochemically induced fractures. Initial experiments were done using a polyvinylidene difluoride (PVDF), polyacrylic acid (PAA), or carboxymethylcellulose (CMC) polymeric binder system and were spin-coated from an NMP solution onto native oxide (SiO_x)-terminated crystalline silicon substrates. The samples were then lithiated to the same extent as control sample of an uncoated SiO_x -terminated silicon anode. For lithiation, $10 \mu\text{A cm}^{-2}$ of current was applied to the working electrode for 60 h using 1.2 M LiPF_6 in EC/EMC = 3/7 (wt%) with 10 wt% FEC electrolytes. The same current density was applied for delithiation with a cutoff voltage of 1.5 V (vs. Li/Li^+).

Plan view SEM images from these PVDF-, PAA-, CMC-coated silicon wafer samples are shown in **Figure 1.1.9.032.20** (middle row). Following the 10th charge-discharge cycle, the SEM plan view images show that the polymeric capping layers based on PVDF-capped silicon wafers exhibit extensive cracking all over the sample, whereas wafers using CMC show far less cracking, and PAA capping layers do not appear to have any cracking. Additional studies confirmed that the same level of lithiation was achieved electrochemically. Using cross-sectional SEM images after fast ion bombardment (FIB) milling, it was also observed that the extent of the amorphous silicon (a-Si) layer (thickness) was different between the samples. The PVDF sample underwent more extensive lithiation-delithiation during the electrochemical cycling as inferred from the thicker a-Si layer (several 100 μm thick) in this sample, whereas in CMC- and PAA-coated silicon wafers, show virtually no a-Si present.

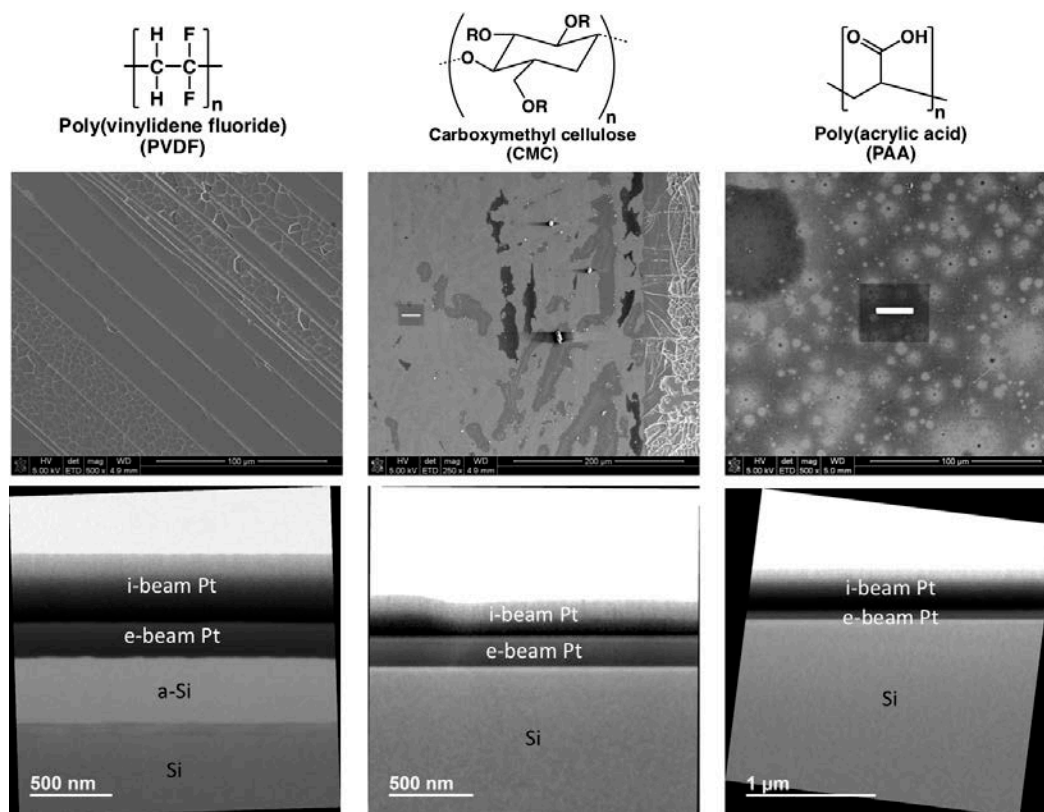


Figure 1.1.9.032.20. TOP: Chemical structures of polymer capping layers used in this study; MIDDLE: Plan view SEM images. BOTTOM: Cross-sectional SEM images after FIB milling. The trench from the FIB milling is seen in the plan view images for CMC- and PAA-capped wafers.

In addition to the FIB SEM studies, we have utilized a Cantilevered Beam Test (CBT) technique to measure polymer adhesion to silicon that was developed for photovoltaic module durability and reliability. This is an advanced version of a conventional peel test, which has been applied previously for assessing the binding strength of a polymer to silicon and correlating with the electrochemical performance. A conventional peel test used to measure adhesion force of a material to a substrate, however, does not account for *subcritical debonding*: when delamination occurs at a finite rate at driving forces below its critical strain energy release rate, G_c . This phenomenon may occur in polymer-silicon systems due to the viscoelastic behavior of the polymer and/or stress-enabled chemical reactions with environmental species, such as electrolyte and humidity. We have used this methodology and applied it to polymer-on-silicon wafer electrodes as shown in **Figure 1.1.9.032.21**, and preliminary data suggests, in conjunction with electrochemical performance data and microscopy data, it can be used to quantify the relationship between the mechanical properties of the surface capping layer and the cracking propagation of underlying silicon electrodes.

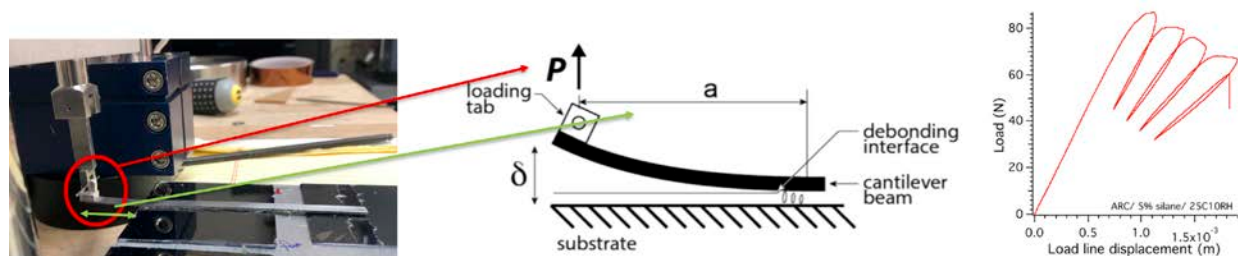


Figure 1.1.9.032.21. LEFT: Cantilever Beam Test (CBT) instrument showing the cantilever bound to a polymer-capped silicon wafer; MIDDLE: Schematic of the single cantilever beam method. RIGHT: Representative load versus displacement plot obtained during a v-G measurement. Load reversals are conducted to extract dC/da (change in beam compliance C as a function of extended debond length a) and obtain G_c values as the debond extends.

Conclusions : In this past year we have undertaken a significant effort studying the various components and properties of slurries and solutions to gain a better understanding of the interactions of silicon and the binder that drive electrode quality. Specific studies have included the solution structures of PAA-binders to understand the role of pH, additives, and polymer morphology. Combined with neutron diffraction, clustering and agglomeration were identified as well as an interesting change in properties when silicon was added to the mixture. In that case the properties of the slurry (i.e. viscosity) were dramatically effected as the polymers interaction with the silicon surface induced structural variations that changed fundamental properties related to shear thinning. Once properly coated it can be noted that the binding strength and coating thickness of the binder have some effect on the underlying silicon fracture properties tied in part to coating homogeneity and probably the binding mechanism used by the pair of materials. Brought together the electrode slurries, electrodes processing science, and the electrochemical evaluation protocols, form a complex problem that need insights across multiple fronts to make advances. This past year significant across-lab advances in our understanding of the electrode slurries and binder interactions has produced more homogenous composite electrodes and a better understanding of the factors that have limited the electrochemical performance of the baseline electrodes.

2. Results: Silicon Surface Modifications

Understanding the electrochemical performance of silicon is dependent on several materials characteristics of the underlying active material. Understanding that the electrochemical process is mediated by the electrolyte-surface interactions, tailoring the surface can provide a pathway towards developing a more stable and robust interface. Within the DeepDive effort, several approaches are under investigation to modify this critical interface via modifications of the underlying silicon rather than by modifications of the electrolyte composition. An example of electrolyte modification may be addition of materials that polymerize to form detached but protective films on the surface, such as fluoroethylene carbonate (FEC), which is a different research pathway than a DeepDive approach of chemically attaching 1) a polymer to the surface (Zhang, Neale), 2) defect elimination in the passivation layer (Lu), or 3) adding electrochemically active interfaces with low oxophilicity to the interface (Tong). This effort supports the electrode effort as it seeks to create an understanding of the interface, active surface species, and viable surface modifications that would feed into to more stable electrode structures and electrochemical performance. In this section, advances and approaches to modifying the surface of the silicon bound within an electrode structure in an electrochemical cell will be discussed.

Functionalization: One of the most direct methods to modify the interface is to utilize the passivation coating as an anchor for a modified chemical species at the interface. While the natural passivation coating of silica has minimal reactivity and thus has limited utility for this effort, the Neale group at NREL has developed methods to scale up hydride-coated silicon particles (designated *H-SiNP*) that possess the requisite reactivity to support

designer chemical modifications. In collaboration with the Zhang Group (ANL), hydride terminated silicon created by a plasma method derived from silane, was used as a base for multiple approaches to surface modification. The general approach, shown in **Figure 1.1.9.032.22**, provides the synthetic route of surface-functionalization. The H-SiNPs were modified with an oligoether-epoxy group $((\text{CH}_2\text{CH}_2\text{O})_n\text{-Epoxy})$ or $(\text{EO})_n\text{-Epoxy}$ via a Pt-catalyzed hydrosilylation reaction.

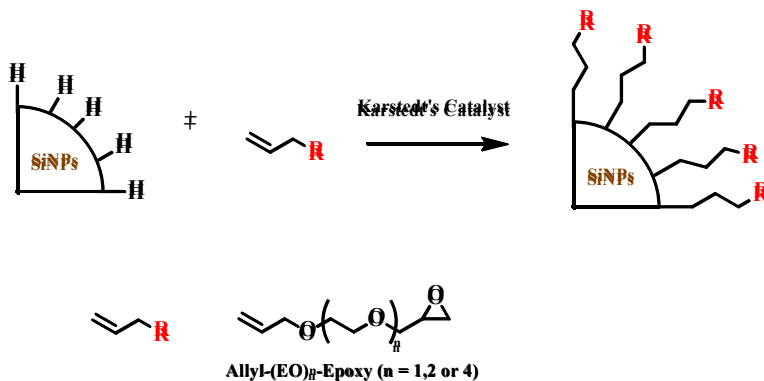
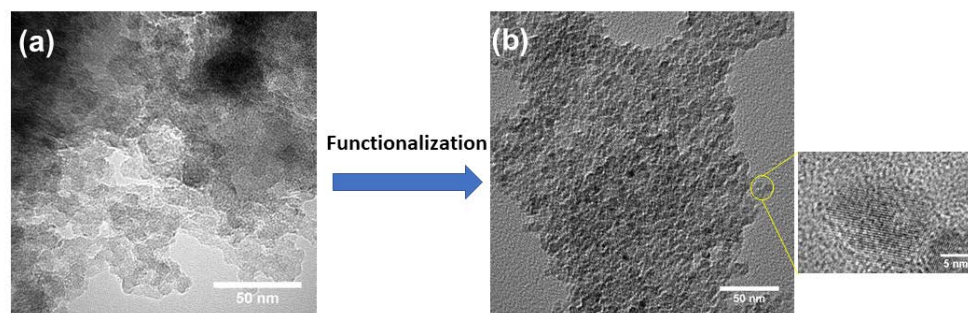


Figure 1.1.9.032.22. Synthesis of surface-functionalized silicon nanoparticles SF-SiNPs

In **Figure 1.1.9.032.23** TEM images of the SiNPs before and after surface functionalization are shown. In the figure it is apparent that the H-SiNPs (as provided) are agglomerated into clusters, while after surface functionalization the particles show a more even distribution with no agglomeration noted. The stability of SiNPs created by surface functionalization was further verified by a dispersion experiment, illustrated in **Figure 1.1.9.032.23**, where surface functionalized SiNP (designated *SF-SiNP*) were dispersed in water. After 24 hours, the sample color and appearance remained unchanged indicating significant stability in the aqueous environment, in contrast, the unfunctionalized H-SiNP when dispersed in water formed translucent solution that precipitated on standing for 24 hours.



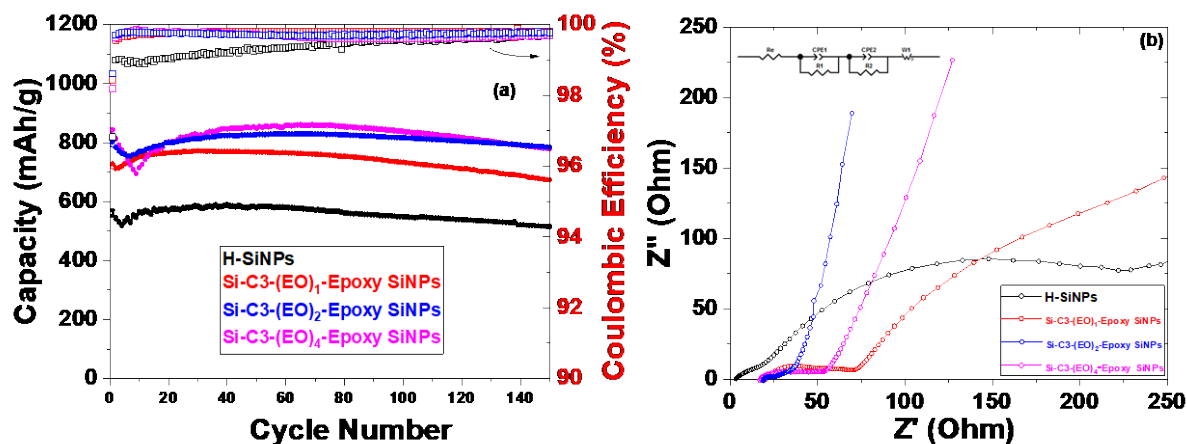


Figure 1.1.9.032.24 Electrochemical performance of Si composite electrodes. (a) Cycling performance and Coulombic efficiency, and (b) Nyquist plots of H-SiNP and SF-SiNP electrodes after 150 cycles.

Table 1. Summary of grafting density, loading density, initial capacity, Coulombic efficiency, capacity retention, and charge-transfer resistance (R_{ct}) of graphite/silicon composite electrodes fabricated using H-SiNPs or SF-SiNPs.

Anode Material	Grafting density (chains/nm ²)	Loading density (mg/cm ²)	Initial capacity ^a (mAh/g)	Initial Coulombic efficiency ^a (%)	Capacity retention (%)	Charge transfer resistance R_{ct} ^b (Ω)
Si-H SiNPs	N/A	1.6	552	96.8	93.5	$R_{ct,1}$: 7.3 $R_{ct,2}$: 178.1
Si-(EO) ₁ -epoxy	5.1	1.6	717	98.4	94.1	$R_{ct,1}$: 19.0 $R_{ct,2}$: 20.3
Si-(EO) ₂ -epoxy	4.2	1.6	803	98.2	97.9	$R_{ct,1}$: 3.2 $R_{ct,2}$: 5.6
Si-(EO) ₄ -epoxy	3.6	1.6	828	98.6	94.3	$R_{ct,1}$: 24.4 $R_{ct,2}$: 10.6

^a 1st C/3 delithiation capacity and Coulombic efficiency

^b EIS measured at the 150th cycle; $R_{ct,1}$ and $R_{ct,2}$ are obtained from the high and intermediate frequency semi-circles.

Figure 1.1.9.032.25 shows the results of SEM/EDX analysis of the created SiNP/graphite composite anodes before and after cycling. H-SiNPs show large particle agglomeration before cycling (Figure 1.1.9.032.25a) and after cycling (Figure 1.1.9.032.24c), whereas the surface functionalized SF-SiNPs are well distributed within the graphitic / silicon active material matrix before cycling (Figure 1.1.9.032.25b) and the same electrode morphology was retained even after 150 cycles, as observed in Figure 1.1.9.032.25d. This morphological difference supports the observed high utilization of the SF-SiNPs material in the composite anode where the better silicon dispersion and a more robust mechanism to prevent agglomeration is enabled. In addition, EDX analysis of the surface films shows that the as-prepared H-SiNPs have more F-rich decomposition products on the surface of the electrode when compared with the SF-SiNP anode. This is indicative that the role being played

by the surface functionalization most likely includes mitigation of the parasitic reactions that occur with the electrolyte during repeated cycling.

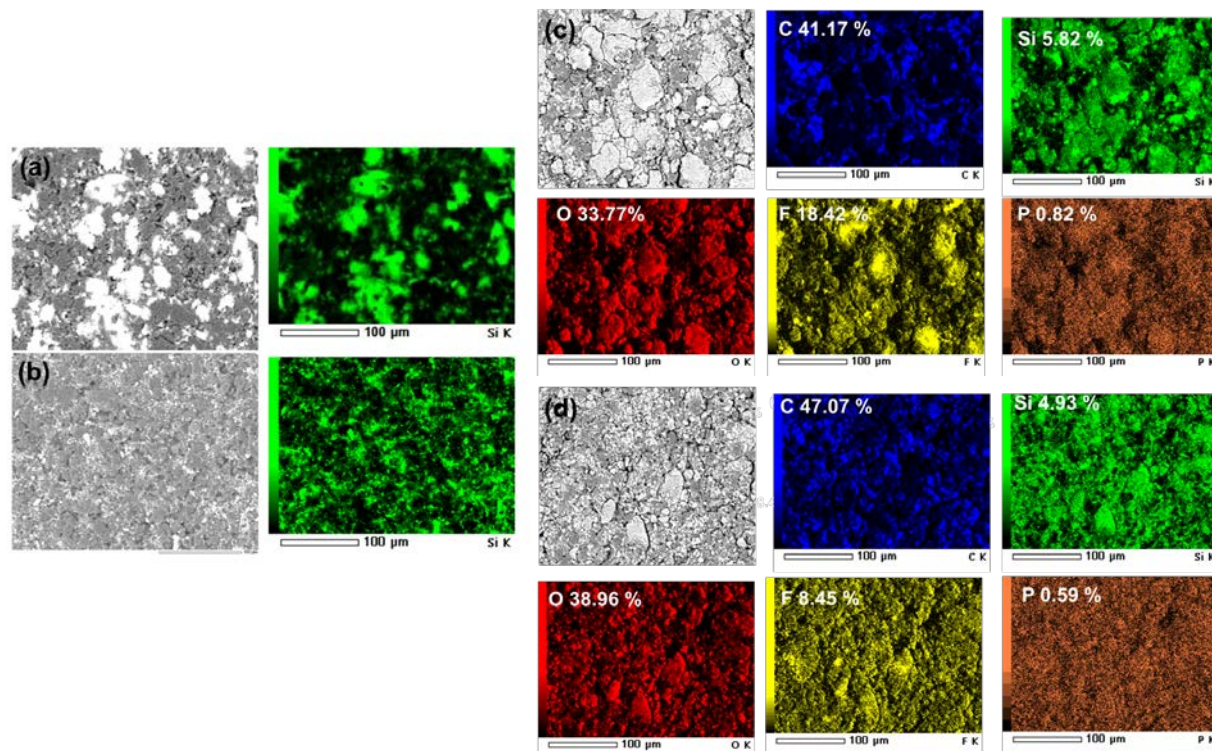


Figure 1.1.9.032.25. SEM images and EDX elemental mappings (colored images) of composite electrodes. (a) H-SiNP anode and (b) surface functionalized Si-C3-(EO)₂-epoxy SiNP anode before cycling, (c) H-SiNP anode, and (d) Si-C3-(EO)₂-epoxy SiNP anode after 150 cycles (C, Si, O, F, and P).

Figure 1.1.9.032.26 shows the electrochemical performance of the H-SiNP electrodes in a half cell. Due to the high reactivity of Si-H group, pristine Si-H terminated SiNPs show both low capacity and Coulombic efficiency. In contrast, after surface functionalization, initial capacities, the Coulombic efficiency and the cycling stability are significantly improved. **Figure 1.1.9.032.26b** shows the F1s XPS data of the H-SiNP anodes after extended cycling. From this we can conclude that the high reactivity of the H-SiNPs is suppressed with surface functionalization as noted by the large drop off in the amount of LiF detected in the F1s XPS spectra for the SF-SiNPs.

Silicon Tin Amorphous Films: An alternative to direct surface modification of nanoparticles is the addition of a compatible lithium-ion conducting phase to the active silicon electrochemical interface. This concept can be evaluated by using a lithium ion conductor that is stable in the same electrochemical window and reversibly lithiates at a higher potential than the silicon. Literature studies on Si-Sn system, notably by the Dahn group, have demonstrated improved cycling stability of the Si-Sn thin film composite compared to Si alone and it meets the criteria proposed as a test system. Electrochemically, elimination of grain boundaries and distinct crystallizes is advantageous for materials mixing and electrode homogeneity. Several methods of synthesis have been evaluated to splat quenching and Si-Sn thin films deposited directly on Cu current collectors by magnetron sputtering. Such thin

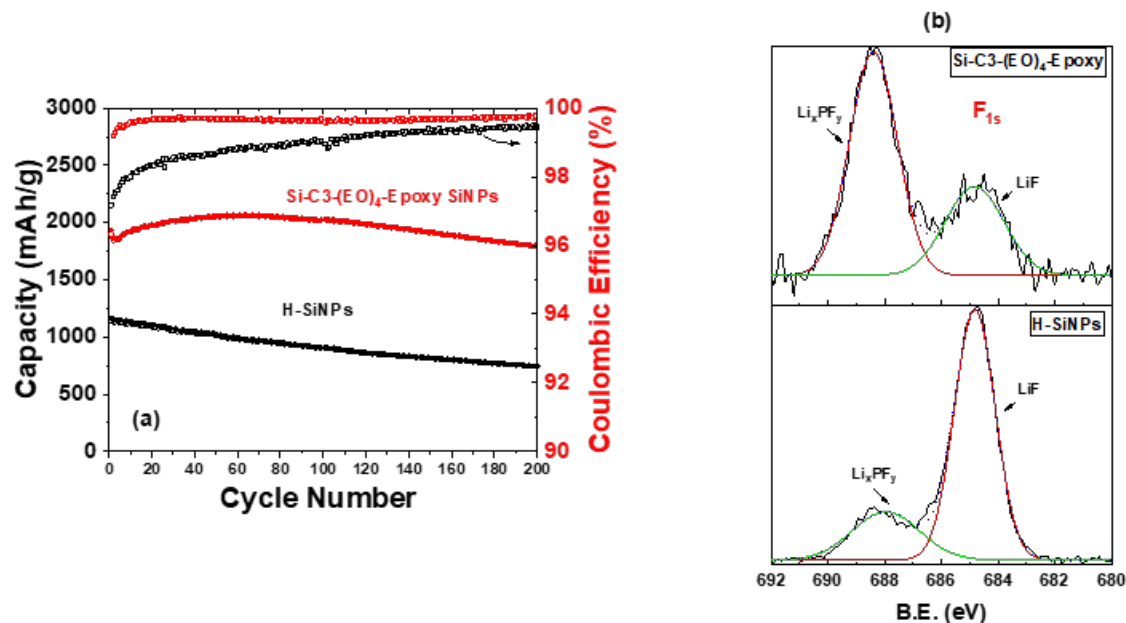


Figure 1.1.9.032.26 (a) Capacity retention and Coulombic efficiency of the pure silicon anodes using H-SiNPs and Si-C3-(EO)₄-epoxy SiNPs as active material, and (b) F1s XPS spectra of H-SiNPs and Si-C3-(EO)₄-epoxy-SiNPs anodes after 200 cycles at delithiated stage.

films free of binder/conductive carbon additive offer the opportunity to enable the effective characterization of solid-electrolyte interphase (SEI) formation, mechanistic understanding of the interfaces, and phase evolution upon electrochemical cycling. The co-sputtered films were characterized by X-ray diffraction (XRD), scanning electron microscopy (SEM), energy-dispersive X-ray spectroscopy (EDS) and electrochemical method to determine the optimal composition with superior cycling performance. Postmortem analysis was carried out to gain constructive understanding on the cycling behavior of Si-Sn and compared to pure Si electrodes.

Previous work has determined that the Si-Sn films sputtered from a single target of fixed composition exhibited better electrochemical cycling stability than Si films of similar thickness (**Figure 1.1.9.032.27**). To allow variation of stoichiometry, the Si-Sn materials were co-sputtering to tune the desired thin film compositions. For these samples Si_xSn_{1-x} composite films were successfully deposited onto a Cu foil current collector by pulsed direct current (DC) magnetron co-sputtering using a 3-inch p-type Si target (99.999% purity) and a 3-inch Sn target (> 99.998% purity). The film composition was tuned by adjusting the deposition power. All the as-deposited films were subsequently stored under vacuum to prevent air exposure and oxidation of the silicon to silica. For evaluation, coin cells were assembled using the films, a Li metal anode, and Gen2 electrolyte. Cells were cycled in galvanostatic mode in the voltage window 1.5 - 0.01 V at C/20. The XRD patterns of the co-sputtered Si_xSn_{1-x} thin films with Si content (x) increasing from 0.45 to 0.87 are shown in **Figure 1.1.9.032.27b**. EDX was used to estimate silicon content, along with a Sn reference. XRD data analysis indicates that at the crystalline Sn peaks are eliminated for x = 0.45 (black line in **Figure 1.1.9.032.27b**) and films outside that range are X-ray amorphous. Note the two strong peaks around 50 and 60° 2θ are from the Cu substrate.

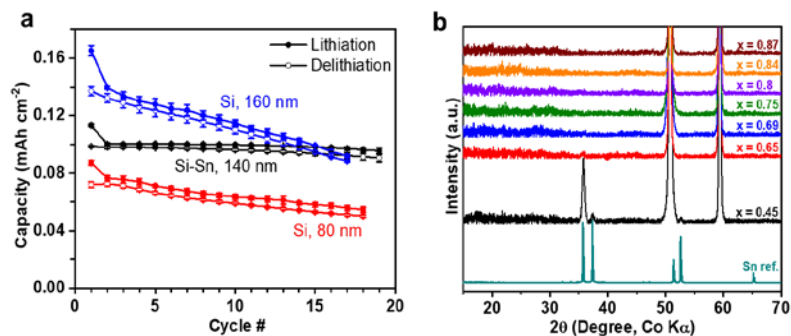


Figure 1.1.9.032.27. (a) Cycling performance of Si-Sn and Si films of similar thickness. (b) XRD patterns of co-sputtered $\text{Si}_x\text{Sn}_{1-x}$ thin films along with Sn reference.

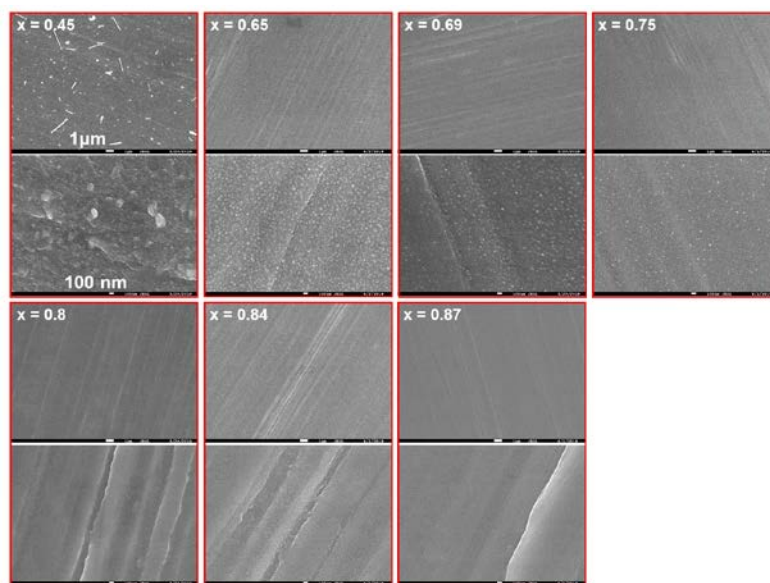


Figure 1.1.9.032.28. SEM images of co-sputtered $\text{Si}_x\text{Sn}_{1-x}$ thin films.

Figure 1.1.9.032.28 shows the SEM images of all co-sputtered Si-Sn films. The upper and lower image in each panel is obtained at a low and high magnification, with a scale bar of 1 μm and 100 nm, respectively. At low

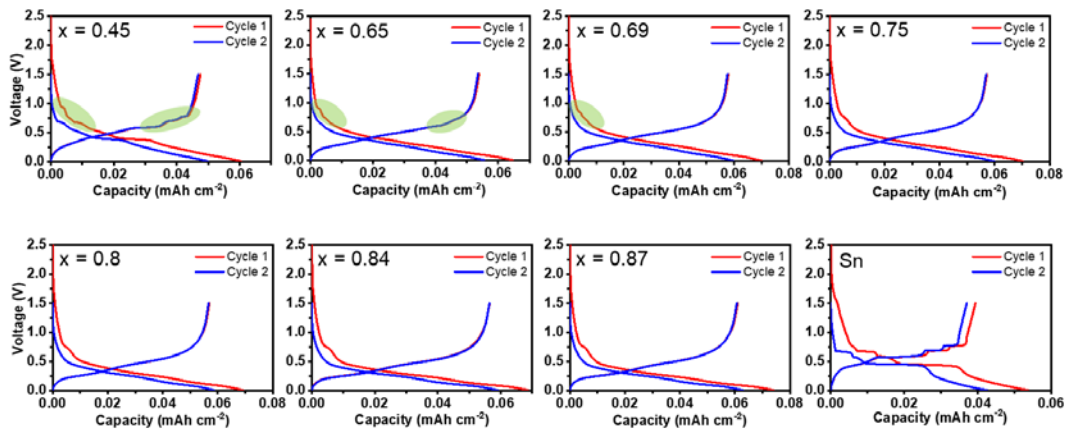


Figure 1.1.9.032.29. Charge-discharge voltage profiles of the co-sputtered $\text{Si}_x\text{Sn}_{1-x}$ thin films during the first two cycles.

magnification (except for $x = 0.45$ which showed crystalline Sn), the films show a striated morphology consistent with the underlying Cu substrate. Higher magnification pictures reveal more variation of morphology. For the

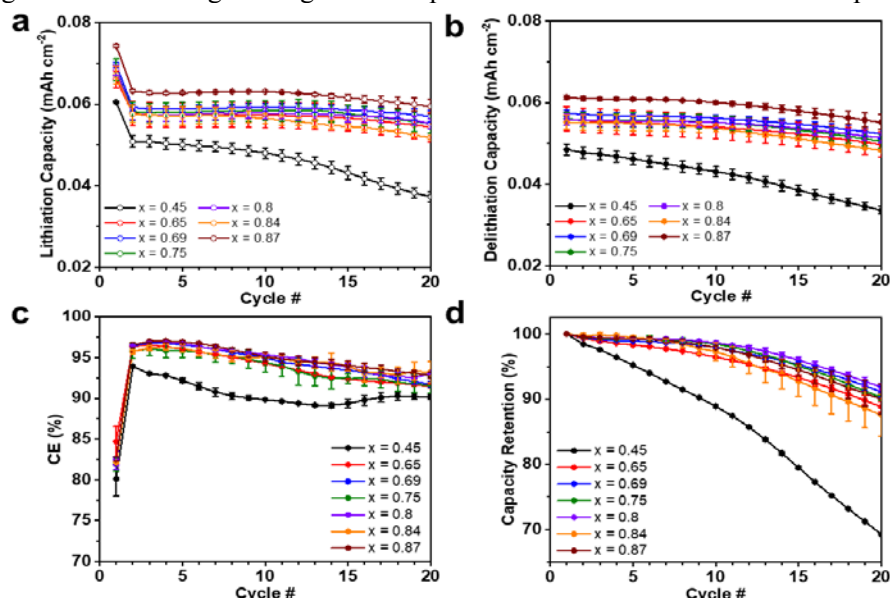


Figure 1.1.9.032.31. (a) Lithiation capacity, (b) delithiation capacity, (c) coulombic efficiency and (d) capacity retention of co-sputtered $\text{Si}_x\text{Sn}_{1-x}$ thin films upon cycling.

films of $0.45 \leq x \leq 0.75$, aggregated particles are observed with increasing Sn content, although the films with $0.65 \leq x \leq 0.75$ appear X-ray amorphous. With Sn content decreasing to ≤ 0.2 ($x = 0.8$), no visible particles are observed; instead, uniform films are obtained with the morphology resembling the Cu substrate.

The Si-Sn films were evaluated electrochemically and the voltage profiles of the Si-Sn thin films and pure Sn reference for the first two cycles are shown in **Figure 1.1.9.032.29**. For low Si content ($x = 0.45$) films, characteristic plateaus of Sn are clearly observed. These characteristic features diminish for films of $x = 0.65$

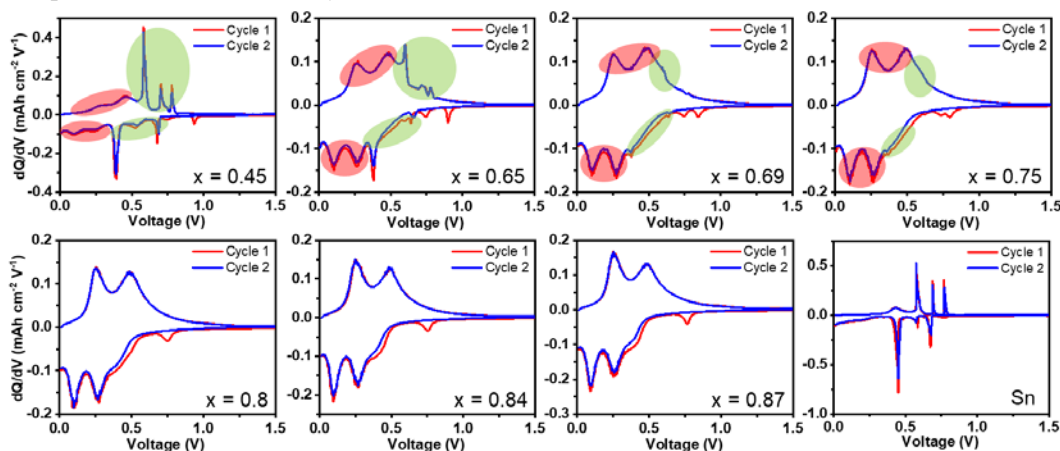


Figure 1.1.9.032.30. dQ/dV plots of co-sputtered $\text{Si}_x\text{Sn}_{1-x}$ thin films during the first two cycles.

and 0.69 and become almost completely invisible for the films with Si contents greater than 75%. The voltage profiles of films with $x \geq 0.75$ are dominated by the typical lithiation-delithiation features of amorphous Si (a-Si) when a-Si is the major component.

The corresponding dQ/dV plots of the Si-Sn thin films (**Figure 1.1.9.032.30**) highlight the role making a homogenous sample in this system aids in preventing phase separation. This was a similar conclusion in the

previous electrode slurry studies that more homogenous samples with better dispersion had better electrochemical properties. The distinct sharp lithiation/delithiation peaks are attributed to Sn for $x = 0.45$, but with increasing Si content, the broad lithiation peaks below 0.3 V and delithiation peaks at ~ 0.3 and 0.5 V, characteristic of a-Si, emerge. For films $> 80\%$ Si, the silicon in a Li_xSn matrix cycles with the features of an amorphous phase and agglomeration and particle growth appear inhibited. A more detailed electrochemical cycling performance of the co-sputtered Si-Sn thin films is given in **Figure 1.1.9.032.31**. The thin film data informed the splat cooling studies underway in conjunction with the Kostecki Group and compositions with approximately 20% Sn are under preparation for scale up to bulk powders.

Carbon-Coated Silicon / Binder Interactions The commercialization of silicon-based electrodes has been hindered by the large volume changes (up to 320%) that result from the insertion/extraction of lithium-ions into/from silicon particles while graphite displays a $\sim 10\%$ volume change. This volume expansion on cycling fractures the silicon particles and increases their surface area, which in turn increases parasitic side-reactions that trap lithium-ions and degrades battery performance. Efforts to modify the silicon particle surfaces to minimize reactivity with the electrolyte and maximize interactions with the polymer binder ranks high among these approaches. Utilizing polymeric coatings to enhance the electronic contact within the electrode matrix is especially important for silicon, given that these particles have an insulating oxide surface layer that forms during material synthesis or storage. Additionally, with charged state reactivity in the cell, surface modification has been proposed as a method to prevent H_2 or other degradation product gases evolution during fabrication processes and during cycling.

To gain a better understanding, X-ray photoelectron spectroscopy (XPS) data was collected from a series Si-based composite electrode containing various surface-modified silicon powders (**Table 2**) obtained from baseline commercial materials vendor Paraclete Energy. The powders were produced by milling and contain Si particles with a mean diameter of ~ 150 nm. The XPS data are for Si particles coated with a thin carbonaceous layer (Si/C), and from Si/C particles with additional coatings based on polyethylene glycol (PEG), polyvinylene difluoride (PVdF), and perfluorooctene (PFO).

Table 2. Si powder description

Powder	Description
Si/C	Si coated with 2.5 wt% carbon
Si/C/PEG	Si coated with 2.5 wt% carbon, further modified with 4 wt% PEG
Si/C/PVdF	Si coated with 2.5 wt% carbon, further modified with 4 wt% PVdF
Si/C/PFO	Si coated with 2.5 wt% carbon, further modified with 4 wt% PFO

In addition to the silicon, the composite electrodes (**Table 3**) used also contain: carbon (for electronic conduction), graphite (for limiting overall electrode expansion) and partially-lithiated polyacrylic acid (Li-PAA, for active binding to the current collector). The Li-PAA was prepared by titrating polyacrylic acid (PAA) with 1 M LiOH in an aqueous solution; exchanging the protons with Li^+ ions reduce coiling of the PAA polymer chains and improves their adhesion to the particles. XPS measurements of the samples were conducted at Illinois (UIUC) using a Kratos Axis Ultra X-ray photoelectron spectrometer (Kratos Analytical, Manchester, UK) with monochromatic Al K_α radiation (1486.6 eV).

Table 3. Electrodes with silicon, Graphite (Gr), carbon black (CB) and LiPAA

Electrode	Si type, wt%	Gr, wt%	CB, wt%	LiPAA, wt%
15 wt% Si / C	Si/C, 15%	73	2	10
70 wt% Si / C	Si/C, 70%	...	15	15
90 wt% Si / C	Si/C, 90%	10

70 wt% Si / C/PEG	Si/C/PEG, 70%	...	15	15
70 wt% Si / C/PVdF	Si/C/PVdF, 70%	...	15	15
70 wt% Si / C/PFO	Si/C/PFO, 70%	...	15	15

Figures 1.1.9.032.32-35 shows XPS data collected from the various electrodes. A comparison of the C 1s spectra are shown in Figure 1.1.9.032.32 of the various components on the electrode surface. The Si 2p regions collected from electrodes are shown in Figure 1.1.9.032.33. The O 1s spectra collected from the electrodes fabricated with the surface-modified silicon particles are shown in Figure 1.1.9.032.34. The F 1s spectra from the electrodes are shown in Figure 1.1.9.032.35. Surface quantification from spectral data on the electrodes is summarized in Table 4. In general, the elemental composition trends are as expected.

Electrochemical button cells were used for the electrochemical tests. Testing was done in either half cells with a Si-composite electrode along (and a Li-metal anode) or in full cells with a capacity-matched NMC532 ($\text{LiNi}_{0.5}\text{Mn}_{0.3}\text{Co}_{0.2}\text{O}_2$) cathode. The electrolyte used was DeepDive standard baseline Gen2+10% FEC.

Table 4. Surface compositions of the electrode samples measured by XPS

Sample	F, at%	O, at%	C, at%	Si, at%
15% Si/C	...	21.3	68.9	9.9
70% Si/C	...	25.7	52.3	22.0
90% Si/C	...	29.7	34.6	35.7
70% Si/C/PEG	...	27.0	45.5	27.5
70% Si/C/PVdF	4.0	28.4	43.2	24.5
70% Si/C/PFO	12.1	23.1	43.0	21.8

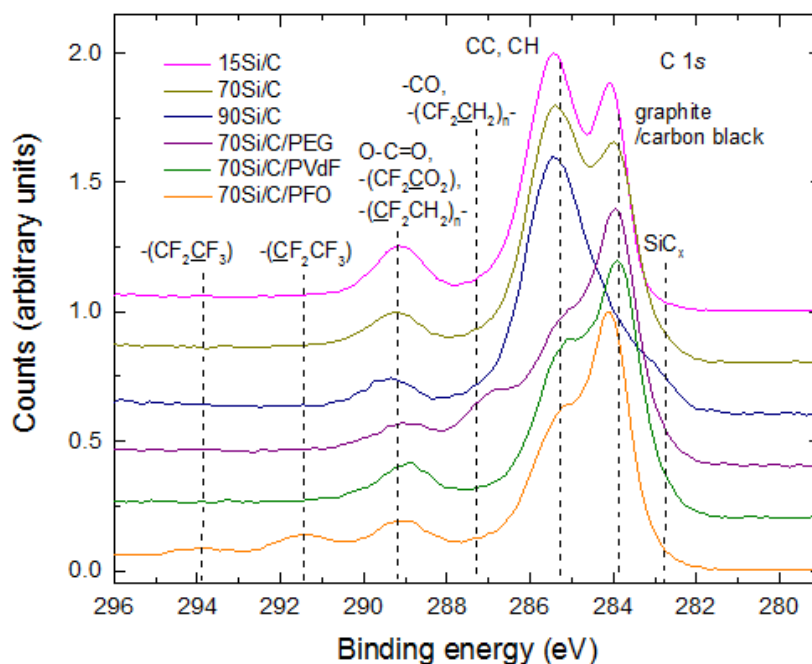


Figure 1.1.9.032.32 C 1s spectra from the 15 wt% Si / C, 70 wt% Si / C, 90 wt% Si / C, 70 wt% Si / C/PEG, 70 wt% Si / C/PVdF, and 70 wt% Si / C/PFO-based electrodes

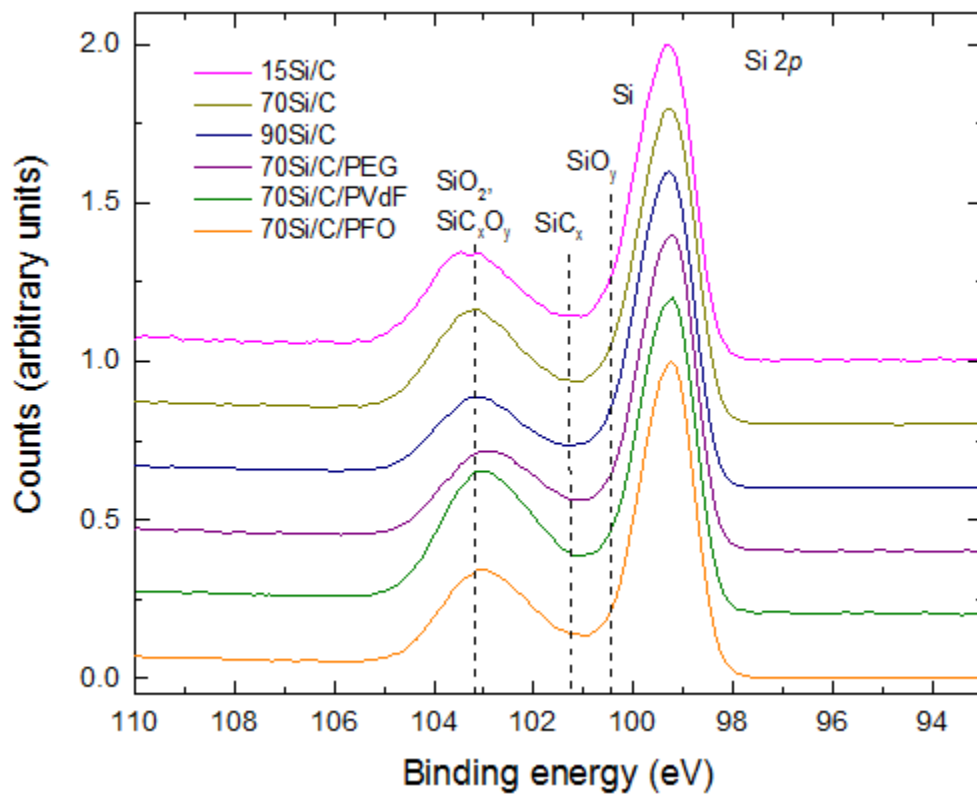


Figure 1.1.9.032.33. Si 2p spectra from the 15 wt% Si / C, 70 wt% Si / C, 90 wt% Si / C, 70 wt% Si / C/PEG, 70 wt% Si / C/PVdF, and 70 wt% Si / C/PFO-based electrodes.

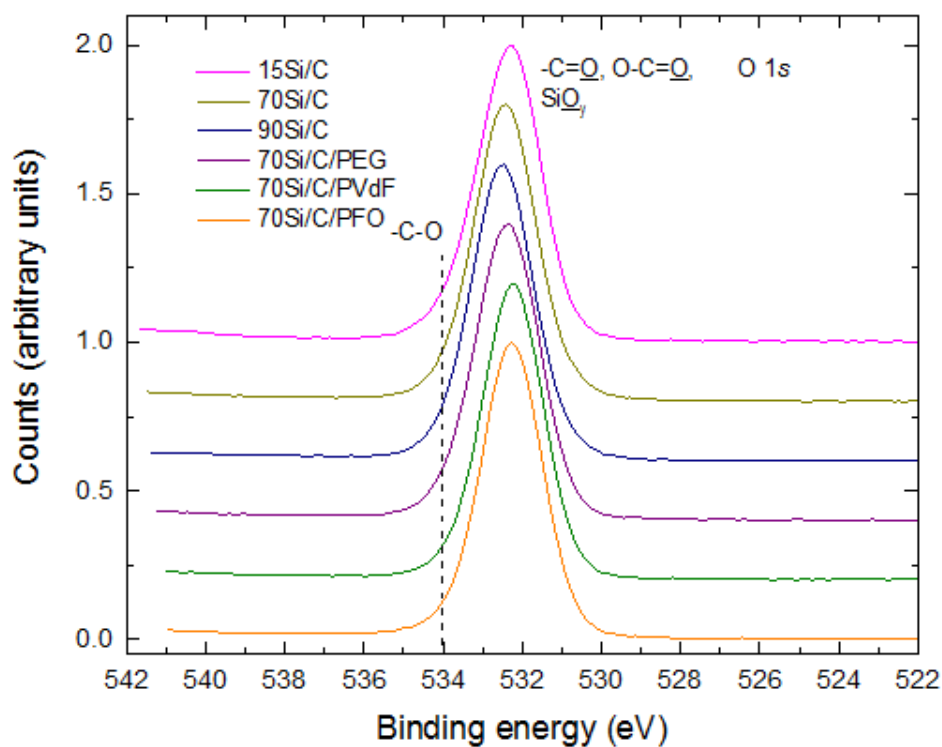


Figure 1.1.9.032.34 O 1s spectra from the 15 wt% Si / C, 70 wt% Si / C, 90 wt% Si / C, 70 wt% Si / C/PEG, 70 wt% Si / C/PVdF, and 70 wt% Si / C/PFO-based electrodes.

Table 5. First cycle capacities and coulombic efficiencies of half cells with Si electrodes

Electrode	Si type, wt%	Lithiation, mAh/g	Delithiation, mAh/g	Coulombic Efficiency, %
15 wt% Si / C	Si/C, 15%	527	460	87.3
70 wt% Si / C	Si/C, 70%	1606	1375	85.7
90 wt% Si / C	Si/C, 90%	1823	962	52.8
70 wt% Si / C/PVdF	Si/C/PVdF, 70%	1554	1264	81.3
70 wt% Si / C/PFO	Si/C/PFO, 70%	2218	1904	85.8
70 wt% Si / C/PEG	Si/C/PEG, 70%	2098	1721	82.1

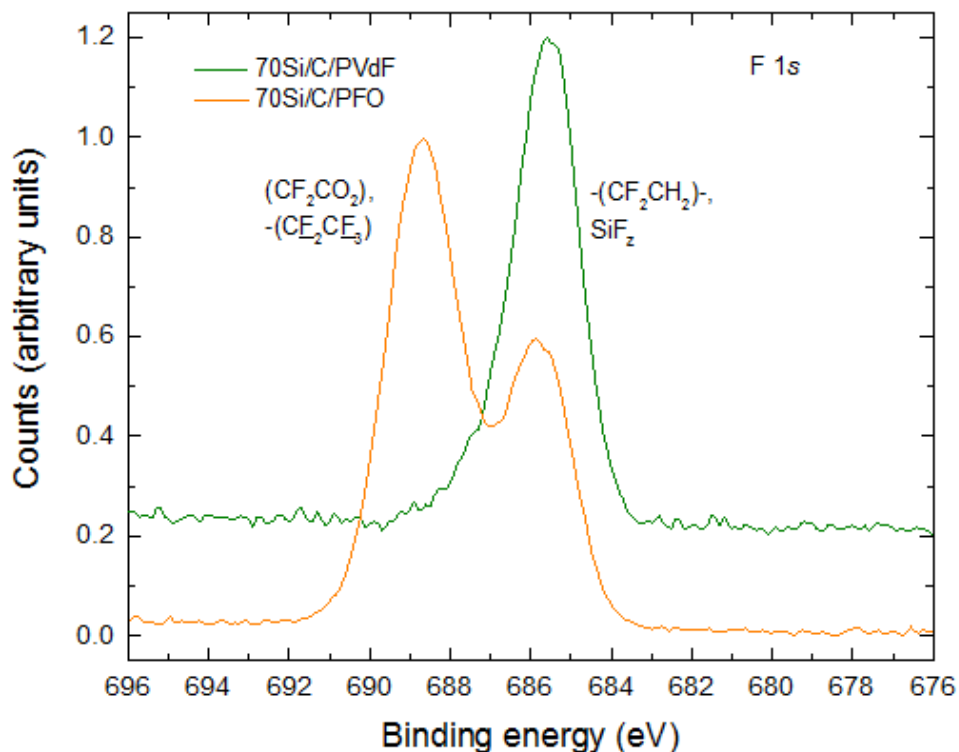


Figure 1.1.9.032.35. F 1s spectra from the 15 wt% Si / C, 70 wt% Si / C, 90 wt% Si / C, 70 wt% Si / C/PEG, 70 wt% Si / C/PVdF, and 70 wt% Si / C/PFO-based electrodes

Figure 1.1.9.032.36 shows the differential capacity (dQ/dV) peak associated with electrolyte reduction during the first cycle and SEI formation; peaks are present for all samples, except 90 wt% Si / C. In all cases, the peak is centered in the 1.0 – 1.1 V range, which is characteristic of FEC reduction. The small variations in peak location and intensity suggest subtle differences in electrolyte reduction (and possibly SEI composition) for the various samples. The apparent lack of a ~ 1.0 V peak for the 90 wt% Si / C sample maybe from the increased polarization (and hence delayed solvent reduction) resulting from the absence of carbon black in the electrode.

The full cells were cycled in the 3.0-4.1 V range; the data from the tests are given in **Table 6** and **Figure 1.1.9.032.37**. The 15 wt% Si / C cell has higher initial discharge capacity than the 70 wt% Si / C and 90 wt% Si / C cells. The capacity differences arise from differences in the 1st cycle coulombic efficiencies, which are 76.1, 67.8 and 50.3% for the 15, 70 and 90 wt% Si cells, respectively. This trend is in line with expectations in line with the adage that “higher the Si content, greater the lithium losses in the solid electrolyte interphase (SEI)”. The absence of C45 carbons explains the low capacity retention (11.2%) of the 90 wt% Si / C cell because active particle isolation becomes more likely. As for the coatings on underlying Paraclete Si particles, PVdF and PFO have small effects on the capacity retention that are within the range of uncertainty. The cell with the PEG-coated particles shows a rapid loss of capacity suggesting that the reactions of PEG with the SEI yield compounds that isolate the active particles. The higher reactivity of the PEG samples on cycling is in line with the observations by Key and Vaughey (ANL) noted last year, that the charged silicon anodes showed heightened reactivity to this class of binders when compared to other available options.

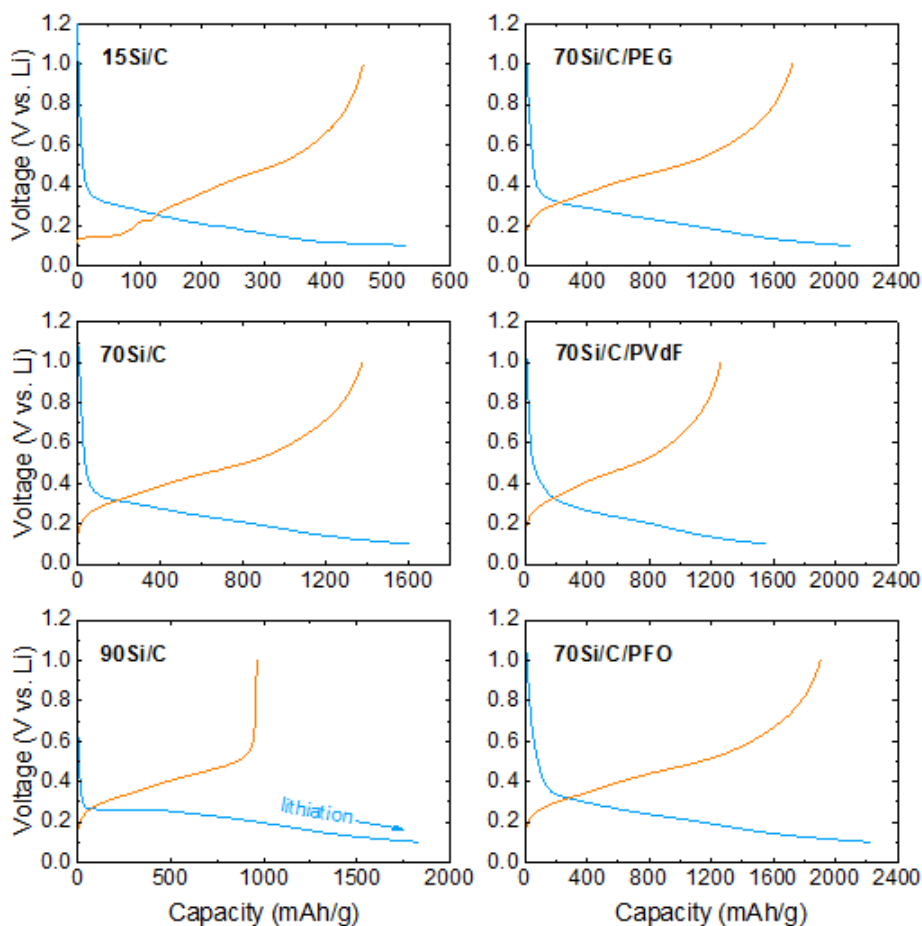


Figure 1.1.9.032.35 Electrode potential changes during the first lithiation/delithiation of half-cells with the 15 wt% Si / C, 70 wt% Si / C, 90 wt% Si / C, 70 wt% Si / C/PEG, 70 wt% Si / C/PVdF, and 70 wt% Si / C/PFO electrodes.

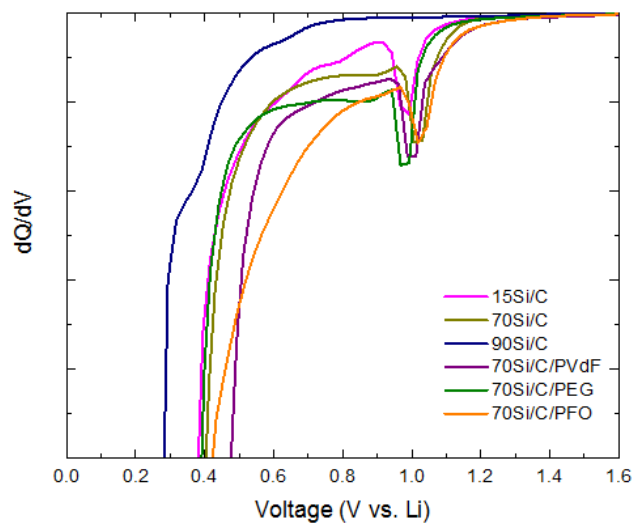


Figure 1.1.9.032.36. Differential capacity (dQ/dV) as a function of voltage during the first lithiation of half-cells with the 15 wt% Si / C, 70 wt% Si / C, 90 wt% Si / C, 70 wt% Si / C/PEG, 70 wt% Si / C/PVdF, and 70 wt% Si / C/PFO electrodes. The peak observed at $\sim 1.0 - 1.1$ V is not observed during subsequent lithiation cycles.

Table 6. Discharge Capacities (1st and 99th cycle) and Capacity Retention of the full cells

Electrode	Si type, wt%	1 st cycle, mAh/g	99 th cycle, mAh/g	Retention, %
15 wt% Si / C	Si/C, 15%	136.4	85.4	62.6
70 wt% Si / C	Si/C, 70%	118.6	79.4	66.9
90 wt% Si / C	Si/C, 90%	93.2	10.5	11.2
70 wt% Si / C/PVdF	Si/C/PVdF, 70%	120.2	74.9	62.3
70 wt% Si / C/PFO	Si/C/PFO, 70%	130.0	86.7	66.6
70 wt% Si / C/PEG	Si/C/PEG, 70%	122.8	21.2	17.3

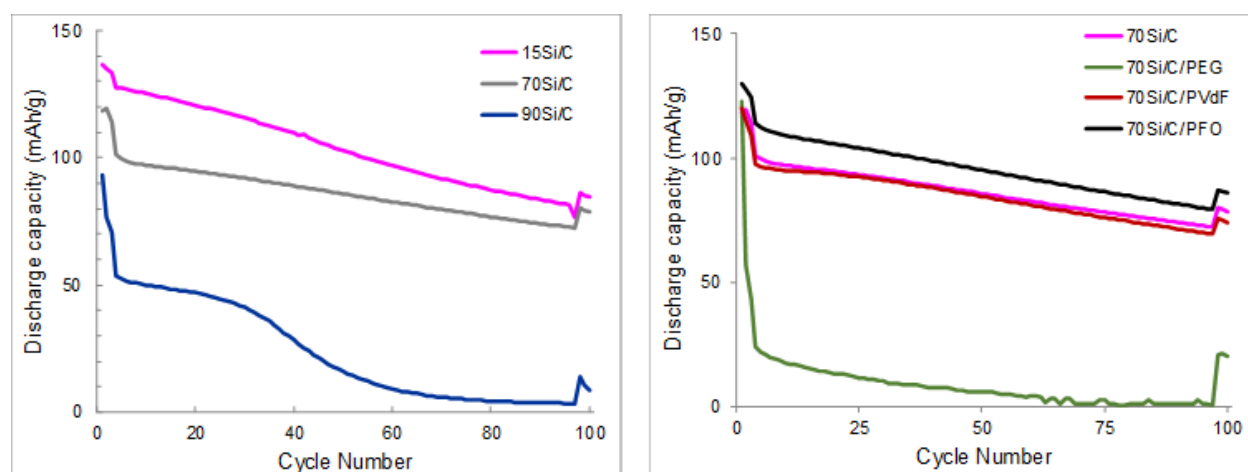


Figure 1.1.9.032.37. Comparing the discharge capacity vs. cycle number for full cells containing (a) 15 wt% Si / C, 70 wt% Si / C, 90 wt% Si / C and (b) 70 wt% Si / C, 70 wt% Si / C/PEG, 70 wt% Si / C/PVdF and 70 wt% Si / C/PFO electrodes. Cycles 1-3 and 97-100 are at a $\sim C/20$ rate, where C refers to the initial C/1 capacity of the cells; cycles 4-94 are at a $\sim C/3$ rate.

Observationally, the XPS data were consistent with expectations with peaks from silicon, the particle coatings, carbons, and binder observed in the spectra. The effect of the polymeric coatings on the silicon were minimal in either cell design scenario used. The best data were obtained for the perfluorooctene (PFO)-coated silicon particles that displayed a higher initial capacity, however, the capacity fade rate for these electrodes were similar to that of the uncoated particles indicating the method of coating and types of polymeric coating materials do not improve the performance of the underlying electrode materials beyond an initial positive effect.

Interfacial Zintl Phase Formation: Whereas the efforts noted above evaluated coatings that were associated with the surfaces of the silicon anode, the incorporation of a material into the surface, to become part of the surface aids in stability and longevity as the extra interface becomes either non-existent or can be described as a gradient. An alternative approach to the surface functionalization via surface attachment with poly-ether groups is the formation of a gradient at the interface that at the surface acts to reduce the redox activity of the electrode. In these silicide systems, the reducing power of the surface species is significant and previous work has shown that the reactivity of these phases with free solvent molecules and binders was a significant side reaction that exacerbated active lithium losses. With the introduction of various multivalent cations, we have identified a pathway that maintains the electrochemical properties of the bulk silicon electrode while reducing the redox activity of the surface, the interface in contact with the electrolyte. Tuning the methods of introduction and

identifying in-situ synthesis methods can lead to control of the reactivity by tuning the reactivity and defect chemistry.

Whereas we previously reported that binary Li-Si phases are reactive against most common solvents and binder materials, Li-M-Si ternary compounds (M= Mg, Zn, Al, Ca) are chemically stable against common electrolyte solvents and they can be formed *in-situ* through electrochemical co-insertion after adding Mg(TFSI)₂ (or salts Zn, Al or Ca) as a second salt into the electrolyte at low concentrations. Mechanistically, it's been noted that the phenomenon changes the traditional Li-Si binary surface chemistry while minimally effecting the electrochemical profiles, capacities, and rate capabilities by stabilizing the interface and reducing side reactions with the electrolytes. Initial half-cell electrochemical testing showed higher capacity, better cycling, and improved coulombic efficiencies with the new electrolyte containing Mg(TFSI)₂ as the secondary salts.

Table 7 Formulations and notations of the electrolytes used in this study.

Notations	Components
Gen2	1.2 M LiPF ₆ in 30 wt% EC + 70 wt% EMC
GenF	Gen2 electrolyte + 10 wt% FEC
GenFM	GenF electrolyte + 0.1 M Mg(TFSI) ₂
GenFZ	GenF electrolyte + 0.1 M Zn(TFSI) ₂
GenFA	GenF electrolyte + 0.1 M Al(TFSI) ₃
GenFC	GenF electrolyte + 0.1 M Ca(TFSI) ₂
GenFL	GenF electrolyte + 0.1 M LiTFSI

NMC532: In a full cell test, two standard CAMP anode baselines (Si+GenF and Graphite+Gen2) were used with appropriate active material loadings to match CAMP NMC532 (LiNi_{0.5}Mn_{0.3}Co_{0.2}O₂) or Li-rich HE5050 (Li_{1.2}Ni_{0.2}Co_{0.2}Mn_{0.6}O₂) cathodes. The electrolyte formulations are shown in **Table 7**. The full-cell configurations were chosen since neither M cation intercalates into graphite nor has an appreciable insertion chemistry related to the selected cathodes. The full-cell electrochemical performance is shown in **Figure 1.1.9.032.38**. Initial analysis of the NMC532 cathode // Si anode cells, cycled between 3.0 V and 4.1 V at C/3 (with 4.1 V holds at the end of each charge cycle) was performed using the GenFM electrolyte (see **Table 7**). When compared to the system without addition of the divalent cation salt, the addition of the divalent cation leads to a higher capacity retention rate of 68% (over 90 cycles) when compared with the baseline GenF electrolytes system, 49% retention (over 90 cycles). While still below the performance of the CAMP graphite anodes (96% retention over 90 cycles), additional improvements are being evaluated in conjunction with multiple SEISTA research teams as, even in these preliminary evaluations, cells using Si anodes have significant increases in energy density, as shown in **Figure 1.1.9.032.38 b,c**. Adding a secondary Mg salt into the electrolyte brought an improvement of ~ 0.15% to the Coulombic efficiency (see **Figure 1.1.9.032.38d**). For its uses in an electrochemical cell, impedance is always considered especially when new materials are being added to the active electrochemical interface in the electrode. We have discovered that when using a Mg-Li mixed electrolyte salts, lower initial impedance after the formation cycles as well as after 90 aging cycles was seen. This may be a result of the lower reactivity of the active interface and the resulting diminished reactions with electrolyte blocking the active surface with degradation products. Formulations that use significantly more Mg-salt additives show no obvious cycling advantages in performance, suggesting that the co-insertion process may be slowed as Mg is isolated as an insoluble salt (i.e. MgO) or, with enough SEI buildup, diffusion to the surface may be inhibited or blocked. The fact that no negative response is detected with a factor of two increase (to 0.2

Mg(TFSI)₂, additional salt may be useful if the mechanism for the concentration drop-off on extended cycling is determined.

LMR-NMC HE5050: To bring more active lithium into the cell design, Li-rich layered oxides (TODA HE5050 with 20% additional Li) were used with an increased voltage cutoff to 4.5V during the initial three C/20 formation cycles for the activation and the removal of extra electrochemically active Li. The additional Li extracted from the cathode can be used to compensate the greater amount of Li consumption during the initial SEI formation on Si anodes, which is commonly referred as the 1st cycle irreversible capacity loss. With this built-in prelithiation, much higher capacities can be obtained with a Li-rich HE5050 cathode // Si anode cell. In Figure 1e, cycling between 3 and 4.1 V using GenFM electrolyte is shown. The high-voltage cutoff of the formation cycles should be high enough that the additional Li available can be extracted to compensate the initial Li consumption losses often seen in non-graphitic anodes. **Figure 1.1.9.032.38 e-g** show that after adding Mg into the GenF electrolyte, the discharge capacities and energy densities of the HE5050 cathode // Si anode full cells increased by a dramatic ~30%, indicating that adding Mg secondary salt is an effective way to reduce the Li losses during the SEI formation. As with the example above using NMC532, the addition of a Mg salt leads to lower initial impedance, slower impedance growth over 90 aging cycles, and a high initial Coulombic efficiency of ~99.4% for silicon, approaching levels usually obtained with graphite-only anodes. **Figure 1.1.9.032.38g** shows the combined effect of using a high Si-content electrode with GenFM electrolyte against a Li-rich HE5050 cathode on the full cell electrochemical performance. The total active material weight specific energy density surpasses both graphite anode and silicon anode baselines by a remarkable 30% over 90 cycles. The cells tested above show stable extended cycling performance in **Figure 1.1.9.032.39**, with ~80 mAh/g_{cathode} capacity after 270 cycles for cells with Li-rich cathodes (33% higher over baseline), and ~55 mAh/g_{cathode} after 270 cycles for cells with NMC532 cathodes (120% higher over baseline). After 270 cycles, TEM/EDX analysis of the cycled Si electrodes taken from Li-rich HE5050 cathode // Si anode cells cycled in a GenFM electrolyte, show a bulk Si:Mg ratio of ~24:1, indicating there is still some Mg left inside of the Si particles after long-term. Similar analysis of the Li-rich HE5050 cathode // Si anode cathode particles after 270 cycles shows minimal Mg presence at the cathode-electrolyte interface confirming that Mg has little influence or opportunity to insert into the cathode. The dramatic increase in performance for lithium limited systems such as NMC532 cathodes and the compounded improvement in performance gained via use of mixed salts and intrinsic prelithiation clearly rationalize further improvements in capacities, cyclabilities, and efficiencies that can be obtained by optimizing other cell components such as binders and Si materials.⁴

Moving to other multivalent salts that support formation of similar Li-M-Si ternary compounds, GenFA, GenFC, and GenFZ electrolytes (shown in **Table 7**) were prepared with Al, Ca, and Zn salts and tested in full-cell configurations. In the case of the zinc-based GenFZ electrolyte, the full cell loses all capacity promptly during the first formation cycle of the cycling protocol, which is most likely due to the intercalation activity of Zn-ion in the cathode.⁵ Conversely, the Al- and Ca-salts like Mg work well in the full-cell configuration. As shown in **Figure 1.1.9.032.38**, using Al-containing GenFA electrolyte leads to a lower coulombic efficiency compared with other electrolytes. When paired with NMC532 cathodes, GenFA-based electrolytes lead to lower initial capacity but better capacity retention than the GenF baseline, which let it outperform the GenF electrolyte after ~80 cycles. When paired with HE5050 cathodes, GenFA shows an initial capacity even higher than GenFM but with diminished capacity retention, which might be due to its high capacity utilization or fast rising impedance. Extended cycles for GenFA shows higher cycling decay and performance degradation when compared to GenFM (**Figure 1.1.9.032.39**). Meanwhile, the GenFC electrolyte (Ca addition) brings similar improved capacities, retention rates, coulombic efficiencies and impedance as in the GenFM electrolyte in NMC532-based full-cell tests, as shown in **Figure 1.1.9.032.38 a-d**. In HE5050-based full-cell tests, GenFC shows much higher capacities, better cyclability, higher efficiencies and lower impedance than GenFM (see **Figure 1.1.9.032.38 e-h**).¹ To date the Ca-containing electrolyte performs better than the Mg-containing electrolyte with initial high-voltage activation process. These GenFC cells show a remarkable ~70% capacity retention after 270 cycles in extended full-cell tests as shown in Figure

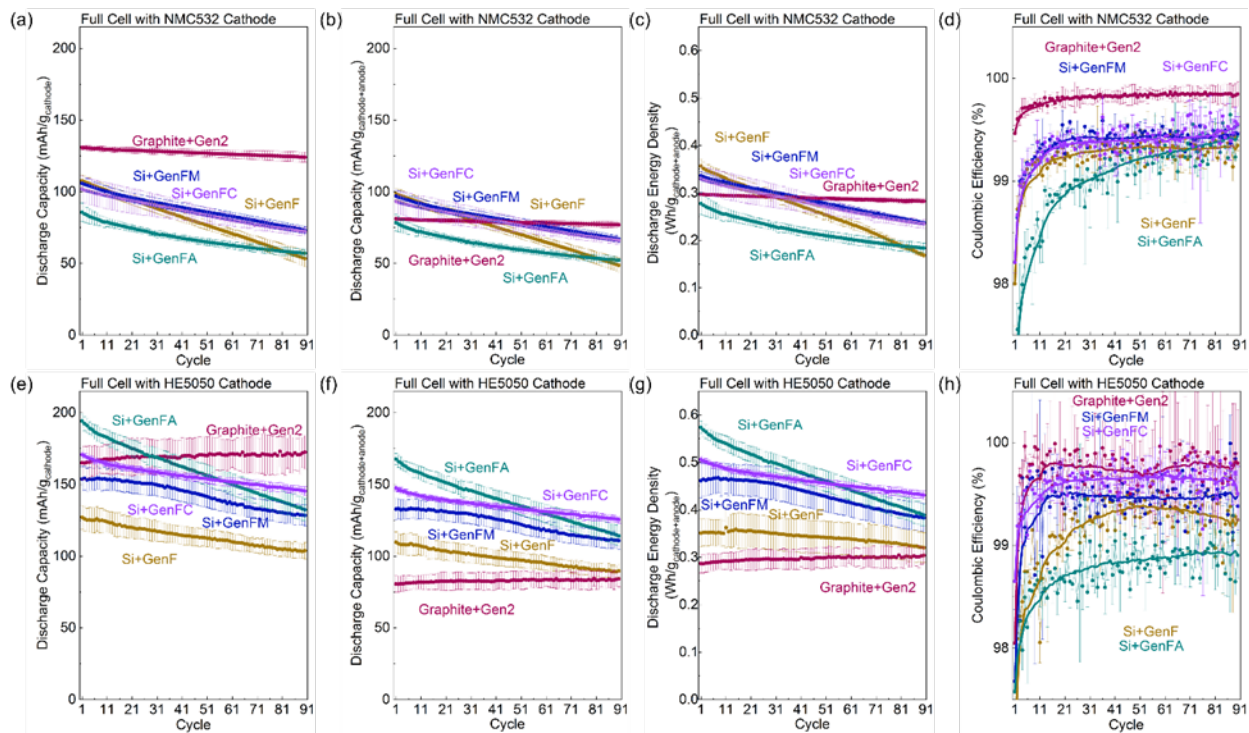


Figure 1.1.9.032.38 Full-cell electrochemical test results. Cells in panels (a)-(d) consist of NMC532 cathodes and Si or Graphite anodes (formation cycles are not shown). Cells in panels (e)-(h) consist of HE5050 cathodes and Si or graphite anodes (formation cycles are not shown). At the end of each charge step the cells were held at 4.1 V until the current dropped below C/50. The discharge capacities in panels (a) and (c) are normalized by the weights of cathode materials (NMC523 or HE5050). The discharge capacities and discharge energy densities in panels (b), (c), (f), and (g) are normalized by the total weights of cathode materials (NMC523 or HE5050) and anode materials (Si or graphite). Error bars represent the standard deviations of at least three measurements for each sample. Trend lines for the coulombic efficiencies in (d) and (h) were calculated by a moving average of 15 adjacent points.

2b. The differences in electrochemical performance trends observed between GenFM, GenFA and GenFA can be due to several factors originating from the complexity of the battery systems, including side reactions, diffusion depth, and role the TFSI⁻ anion plays in SEI stability. Joint studies between Argonne, ORNL, and NREL are addressing these issues are underway and taking advantage of the unique resources each possesses.

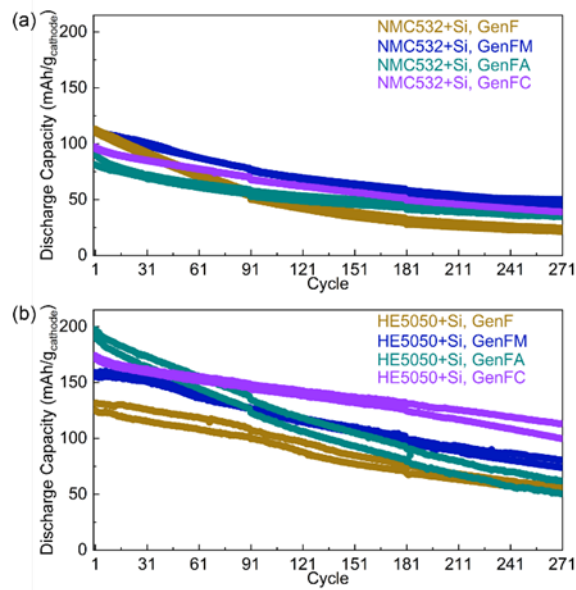


Figure 1.1.9.032.39. Discharge capacities of full cells using GenF, GenFM, GenFA, and GenFC electrolytes with extended cycles. (a) The full cells consist of NMC532+Si electrodes were cycled between 3.0 and 4.1 V at C/3 after three formations cycles between 3.0 and 4.1 V at C/20 (formation cycles are not shown). (b) The full cells consist of HE5050+Si electrodes were cycled between 3.0 and 4.1 V at C/3 after three formations cycles between 3.0 and 4.5 V at C/20 (formation cycles are not shown). At the end of each charging process during aging cycles the cells were held at 4.1 V until the current dropped below C/50. Two cells were tested for extended cycles on each cathode to show that the lifetime of the full cells are repeatable.

Zintl Electrolyte Properties: As seen, significant changes to the active electrochemical interface are observed electrochemically and physically upon addition to the electrolyte of small multivalent cations. EQCM investigations seek to assess role the cations added play in changing the electrolyte equilibriums and carrier species. Samples containing Mg²⁺ and Zn²⁺ cations in the electrolyte were evaluated against a Si thin film anode, to distinguish the early stage SEI formation from Si lithiation. Data were compared to the control electrolyte, Gen2+10% FEC.

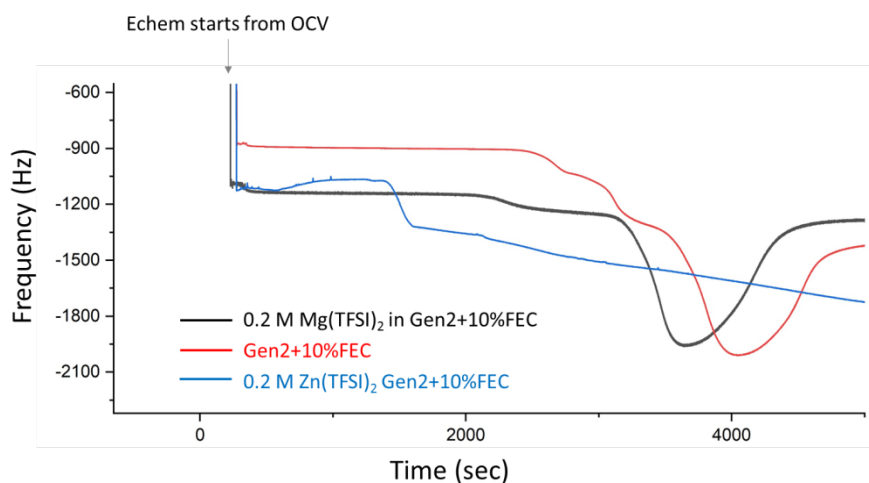


Figure 1.1.9.032.40. Frequency shift for the early SEI formation for the 0.2 M Zn(TFSI) and 0.2 M Mg(TFSI)₂ as electrolyte additives to the baseline electrolyte (Gen2+10%FEC) on a Si thin film anode. Lithiation depth is 0.115 V.

The electrochemical performance of Si thin film anode with DeepDive GenF baseline and either 0.2 M $\text{Zn}(\text{TFSI})_2$, or a 0.2 M $\text{Mg}(\text{TFSI})_2$ as electrolyte additives were compared. Data in **Figure 1.1.9.032.40** presents the frequency shift from OCV to the first lithiation. An EQCM measurement weighs the electrode as it cycles and

combining that information with the electrochemical signal, a value for the SEI weight and porosity can be deduced separate from the weight gained by addition of lithium to the silicon. For these representative cations, it can be seen that early stage SEI formation weight is highest for the Zn (GenFZ) system, and is the least for the Mg (GenFM) system. This result suggests that the SEI formed in the presence of a Mg additive is thinner than the SEI seen in similar studies for baseline GenF electrolytes. Specifically, for the Zn system, no obvious current signal is detected for the first 2 electrochemical cycles suggesting no lithiation of Si is occurring down to 0.4V, as shown in **Figure 1.1.9.032.41**. This is consistent with the previous GenFZ cycling studies where rapid loss of capacity was observed. Compared to other possible cations, the Zn system is easiest to reduce to the metal and has a stable binary Laves Phase (Li_2Zn) that may play a role in removing active lithium if this poor electronic conducting phase plates out at an active interface. From OCV to the lithiation of 0.4 V, only capacitive current is detected and there is no lithium intercalation to Si, however, there is mass accumulation at the Si electrode. Pushing the electrode to lower potential (from to 0.115V from 0.4V), lithiation of Si started with clear intercalation and de-intercalation observed and the corresponding reversible mass change is detected at the same time.

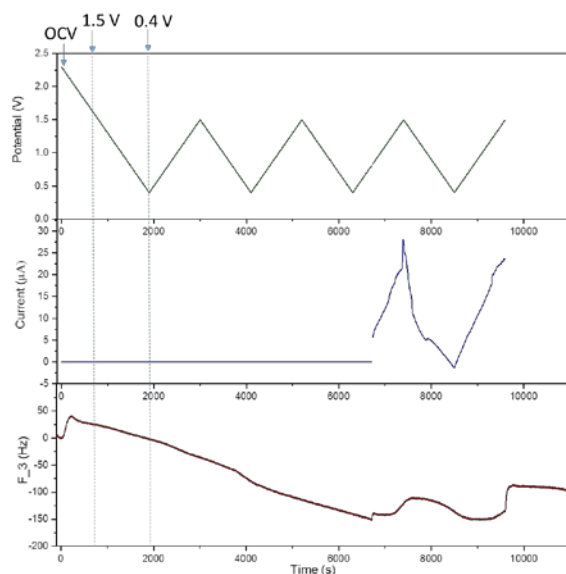


Figure 1.1.9.032.41 Voltage, current and frequency versus time plots of the early SEI formation of $\text{Zn}(\text{TFSI})_2$ additive into the Gen2 electrolyte from OCV to lithiation depth of 0.4 V.

Conclusions: The active interface between silicon and the electrolyte is the critical interface for SEI formation, particle isolation, agglomeration, and cell-based reactivity in general. In this section multiple efforts have been undertaken to examine the diversity of ways to modify this critical interface. In SEISTA, the initial goals included development of a better understanding of the role the natural passivation layer of silica plays in cell chemistry and electrochemical performance. Based on numerous spectroscopic studies and evaluations, the pathway from silica thru lithium silicate formation to eventual dissolution (dispersion) was identified and efforts at control were evaluated. In the DeepDive effort, the main multi-lab focus has been on system level variables and a more active stance with regard to material modifications. Work by Zhang and Neale has focused on

creating a more active surface by using a silane as the source of silicon. This yields a hydride terminated surface that is amenable to controllable substitution reactions. Addition of poly-ether groups has resulted in a more homogenous and dispersed nanophase sample as the surface functionality now plays the role of buffer in addition to assisting in local lithium cation transport. In a similar manner, another joint study with SEISTA has focused on using cation additives that diffuse into the surface of the charged anode to drastically reduce the reactivity towards other cell components, notably the binder and electrolyte solvent. With the in-situ formation of ternary Zintl phases, such as $\text{Li}_{14}\text{MgSi}_4$ and $\text{Li}_{14}\text{CaSi}_4$, redox activity of the surface silicon is eliminated while the close structural relationship to various lithium silicides helps mediate the formation of internal interfaces. The addition of a small amount of Mg or Ca can be readily observed to increase the Coulombic efficiency and extend cycle life significantly, especially in conjunction with a high capacity cathode such as the lithium-rich NMC materials. The performance boost is supported by EQCM data that shows the SEI formed from the Mg-containing electrolyte on silicon was much thinner than the SEI from a standard baseline Gen2 cell; indicative again of the role eliminating the redox activity of the surface silicon has on reducing electrolyte reduction reactions. Additional studies highlighting surface protection schemes, such as encasing the active silicon in an amorphous tin matrix or carbon coating, have also been evaluated. While the tin matrix studies are more analogous to the Zintl phase work, their lack of interdiffusion creates internal interfaces. As noted in this section, several ways have been identified to overcome these issues, notably RF sputtering and splat cooling, that are capable of making amorphous mixtures that do not crystallize and phase separate on cycling. Overall, controlled surface functionalization is a viable method to limit surface reactivity that drives low Coulombic efficiency and side reactions that lose active lithium. Two strategies have been examined in detail and shown promise. Addition and attachment of poly-ethers to the surface is promising as it can alleviate electrode level issues associated with particle agglomeration. While supplies are limited, mainly in the context of the sample sizes required to make a large-scale laminate run at CAMP, scale up studies of the process on commercial silicon have been initiated by Jiang and Zhang. Zintl phase studies continue and collaborative efforts at NREL, ORNL and ANL have identified research pathways and insights that are helping to better understand the limitations and process issues.

3. Results: SEI Stability

Soluble SEI Components: The solid electrolyte interphase (SEI) formed during the cycling of lithium-ion batteries (LIBs) by the decomposition of lithium salt and solvent molecules plays a crucial role for the device performance. On extended cycling these insoluble species precipitate on the active surface, forming the protective SEI layer. In graphitic carbon systems this layer is relatively stable as the lack of significant volume expansion and bond breaking is missing as a driving force when compared to other possible anode systems. With this different mechanism in mind, the SEI formed by silicon (or other main group elements) is different than seen with carbons and tend to have a larger percentage of inorganic phases. In addition to composition, several reports that monitor the SEI as a function of state of charge (i.e. EQCM) have noted that the SEI thickness is not consistent. As lithium is removed on discharge, the SEI thins out. This has typically been assigned to loss of soluble SEI species. However, the identification of these low concentration species is problematic as they are chemically similar to one another, may draw upon minority species in the electrolyte (i.e. fluoride anion), or may react with the cathode. Since these species are critical to understanding the cell cycling profiles in full cells, a study of the wide variety of electrochemical pathways and development of facile analytical methods for chemical characterization of SEIs is needed. With this in mind, a gradient polarity solvent wash (gradient wash) technique

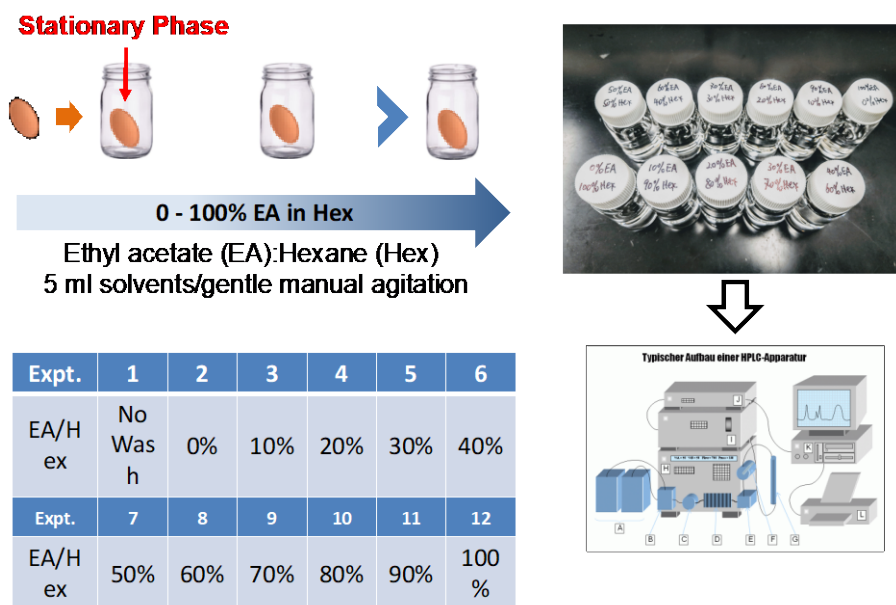


Figure 1.1.9.032.42 Schematics of the gradient polarity solvent wash technique.

involving the use of solvents with gradually increased polarities is employed to sequentially remove different SEI components from electrode surfaces and near surface has been developed and used to identify these low concentration soluble species. A primary identification tool is Fourier Transform Infrared (FTIR) spectroscopy to quickly characterize the SEIs composition and products isolated. This study presents a new concept of rationally controlled solvent wash technique for electrode surface analysis that can selectively remove targeted components with gradient wash off the targeted electrode surface by adjusting solvent polarity to reflect the different solubility requirements of the species that may range from neutral aliphatic species to ionic salts (see **Figure 1.1.9.032.42**). The gradient wash of electrodes was performed in glass vials, where the electrodes were immersed under 5 ml solvents with gentle manual agitation. The solvents used were 0% to 100% volume ratio a polar ethyl acetate (EA) solvent in a non-polar hexane (Hex) solutions with 10-percent intervals (*i.e.* 0%, 10%, 20%, 30% EA/Hex, *etc.*). After rinsing, the electrodes were immediately dried and stored under vacuum until FTIR characterization.

Analysis of the SEI materials and near SEI materials produced using a polar methacrylate additive under different electrochemical conditions were separated by a gradient wash as described. Cu electrodes were cycled with a Gen2 electrolyte (1.2M LiPF₆ with a 3:7 ethylene carbonate/ethyl methyl carbonate (EC/EMC) containing the additive. The methacrylate additive was chosen as it is a partially reduced species similar in structure and composition to the electrolyte solvent breakdown products seen in literature studies. With a binary solvent system of a non-polar solvent and a polar solvent at various ratios, it is possible to selectively remove different SEI components formed on cycling. The electrode surfaces before and after each wash protocol are characterized with FTIR for identification of the decomposition products.

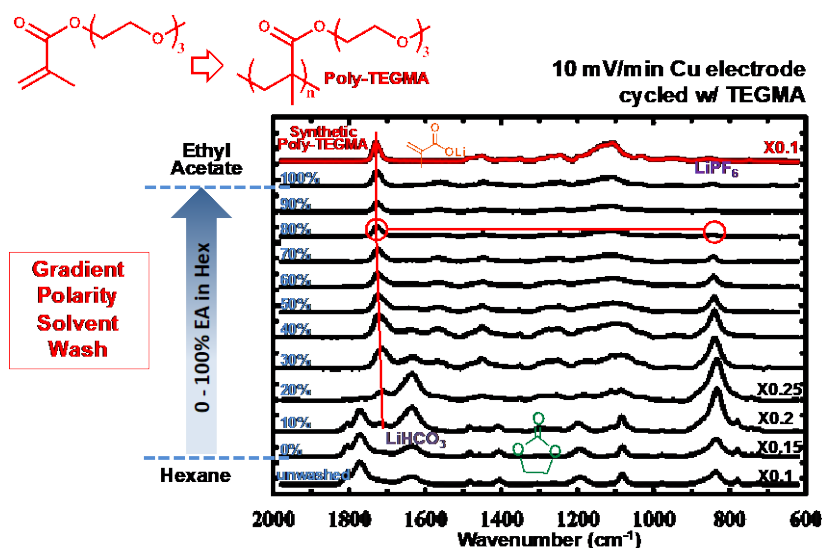


Figure 1.1.9.032.43. Gradient polarity solvent wash was applied to a Cu electrode polarized to 10 mV Li/Li+.

The TEGMA additive, structure shown in **Figure 1.1.9.032.43**, produced a poly-TEGMA film on the Cu electrode surface, which, due to its high polarity, did not resist adsorption of residue electrolyte (EC/EMC:LiPF₆ solvates, 1809, 1780, 1269, 1196, 1082, 833 cm⁻¹) and Li₂CO₃ (1510, 1419 cm⁻¹) as shown in **Figure 1.1.9.032.43**, Spectrum 1. The poly-TEGMA layer was fully exposed after gradient wash with 0-30% EA/Hex solvents. This polar polymer film also survived all remaining washing steps. Its chemical composition was confirmed with the synthetic sample. The removal of electrolyte species with 0-30% EA/Hex solutions is consistent with the case of the base electrolyte. It is worth noting that the carbonyl peak for poly-TEGMA at 1726 cm⁻¹ presented a slight red shift before removal of lithium salt species due to solvation effect.

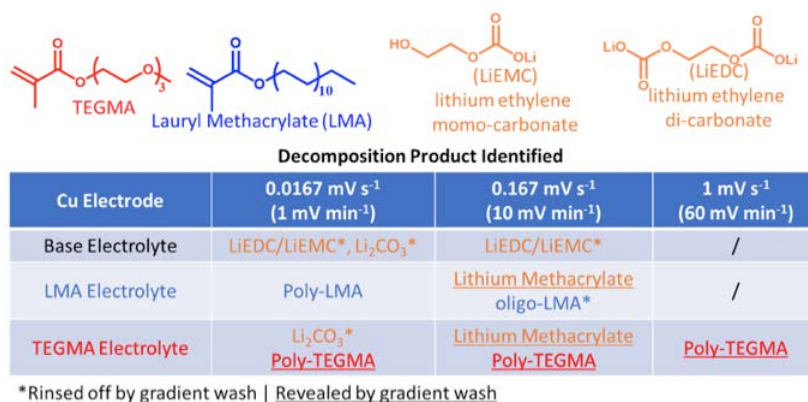


Figure 1.1.9.032.44 Three different scanning rates of CV at 1, 10 and 60 mV min⁻¹ were applied to the Cu electrodes respectively with baseline electrolyte and two additives-based electrolytes. The Cu surface species vary due to both the additives and scan rates.

The scanning rate or the potential step-down rate from 3V to 50 mV has a significant impact to the surface film (SEI) and near surface species formation. At slow to mediate rate of 1 to 10 mV min⁻¹, the baseline electrolyte (EC/EMC: LiPF₆) facilitates the formation of LiEDC/LiEMC salts on the Cu surface. In the two additives-based electrolyte containing systems, they are predominantly additives derived polymer films on the Cu surface instead of lithium salt species. The species on the Cu surfaces can be clearly observed with gradient wash technique. However, when the voltage step rate is 60 mV min⁻¹, the Cu surface are free of deposition of decomposition products with the baseline electrolyte. A highly polar TEGMA additive tends to stick to the surface of the Cu at this fast scan rate. Products identified to date by FTIR as shown in **Figure 1.1.9.032.44**. Therefore, the chemistry of SEI formation is dependent on the reaction rate, where lower lithiation rate favors the formation of lithium salts on the electrode surface, and faster rate promote the formation of polar organic decomposition products.

Besides the solvent polarity gradient techniques developed to date, SEI formation and species identification using a rotating ring disk electrode (RRDE) design rotating unit (with bi-potentiostat) has also been adapted as an analysis method. In conjunction with the ANL and ORNL materials group, several model samples of 50 nm sputtered Si thin films on the Cu disk RRDE tip were created. Notably the simplest baseline sample of Si on Cu did not maintain adherence to the substrate during measurements, however addition of a titanium or chromium adhesion layer onto the Cu gave more stable sputtered Si thin films. As our method development baseline, we have focused on the Si N-type doped disk electrode sample rather than a model silicon electrode on Cu. This combination avoids binder and carbon artifacts in the electrochemistry and instead focus on the pure SEI on Si surface, in a similar manner to the Si-Sn thin film studies allowed for good cycling and diagnostic studies to be developed with a simpler electrode design.

The SEI on the Si N-type electrode surface was grown using a variety of different protocols. First, no protracted growth of SEI was done, a ‘native’ SEI, the second SEI was a 1-cycle study sample grown at 6 μV/s down to 10 mV, and back to 1.5 V, and thirdly, an SEI formed using fast-frequency methods. This last sample was created by sweeping the voltage of the Si N-type electrode disk at 100 mV/s for 10 cycles between 0.01 V to 1.5 V. Following SEI growth, a ferrocene probe molecule was added to the electrolyte (10 mM) as a source of an electrochemical signal and tested at the silicon SEI formed using RRDE method to assess the properties related to molecule partitioning. The electrolyte was Gen 2 with 10% FEC (distilled; dry no water).

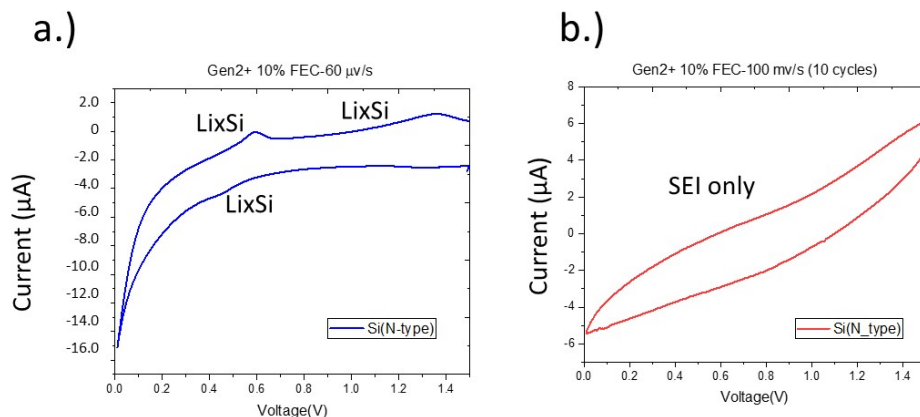


Figure 1.1.9.032.45. Si N-type disk electrode voltammetric results shown for the reductive side of the voltage window where SEI first cycle is shown. (a.) Slow CV at 6 μV/s between 0.01 to 1.5 V vs. LiLi⁺ RE/CE electrode. (b.) Fast frequency electrode disk sweeping at 100 mV/s for 10 cycles between 0.01 to 1.5 V vs. LiLi⁺ RE/CE electrode.

In the analysis part of the experiment, the RRDE was rotated at a variety of speeds in 150 mL of electrolyte in order to sweep away any products from the Si N-type disk to be subsequently electrochemically oxidized or

reduced at the Pt ring electrode. The disk and the ring voltage were simultaneously swept at 2 mV/s from OCV (~ 1 V) to 4.2 V cutoff vs. Li/Li⁺.

Figure 1.1.9.032.45 shows the first sweep i-V curves for the Si N-type disk electrodes in Gen2 + 10% FEC electrolyte. In the ‘native’ SEI, no low voltage sweep was conducted. In (a.), reduction current is seen indicative of SEI formation and some lithiation of Si occurs. For (b.), the fast frequency (*ff*) sweep, the current is roughly the same magnitude, but the CV is featureless. This indicates that little to no lithiation of Si occurs, because of its slow reaction. With this *ff* method, it is expected that the SEI is porous and thick, as it has had no time to age, condense, and collapse. In contrast, for the slow sweep voltage (6 μ V/s), the SEI should be compact and smoother with tighter coverage.

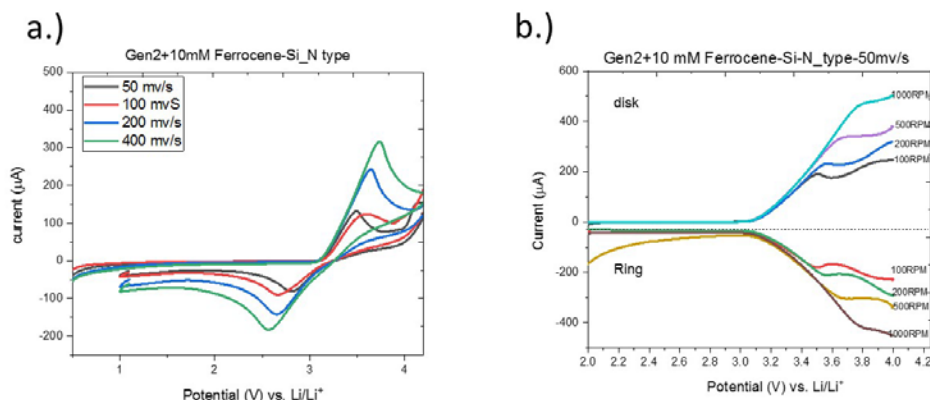


Figure 1.1.9.032.46. (a.) Si N-type disk electrode voltammetric results shown for the oxidative side of the voltage window with 10 mM ferrocene in GEN2 + 10% FEC. (b.) RRDE result showing the limiting current on the Si N-type disk and the Pt ring response to oxidation (disk) and reduction (ring) of ferrocene as a function of rotation rate.

The CV response (i-V curve) at the Si N-type electrode in the presence of ferrocene (10 mM) is shown in **Figure 1.1.9.032.46**. Essentially the voltammetric process is near ideal. Current increases linearly as a function of $v^{1/2}$. In addition, the RRDE output is also ideal. This result suggests that the SEI is ‘native’, very thin, and ferrocene can exchange electrons in a fairly facile way with the underlying Si N-type (conductive) electrode interface.

When the thicker SEI is present on the Si N-type electrode (results in **Figure 1.1.9.032.45**) either in compact form, or porous form, the ferrocene redox response is much less ideal than ‘native’ SEI, thus indicating poor charge transfer through the SEI to react with the ferrocene. **Figure 1.1.9.032.47** indicates that the porosity of the SEI is greater for the SEI formed with *ff* methods. An example of the data is the ring current at the Pt is more defined for **Figure 1.1.9.032.47** which indicates that an oxidized form of ferrocene has partitioned into and out of the SEI and reacted with electron exchange within the SEI. Moreover, for the Si N-type disk current (limiting for 100 mV/s, **Figure 1.1.9.032.47**) at 1000 rpm (green), the limiting value is about 550 μ A, while in **Figure 1.1.9.032.47a**, the current (green trace) is about 330 μ A. Clearly the charge transfer reaction at the SEI is hindered for the compact version versus the porous one.

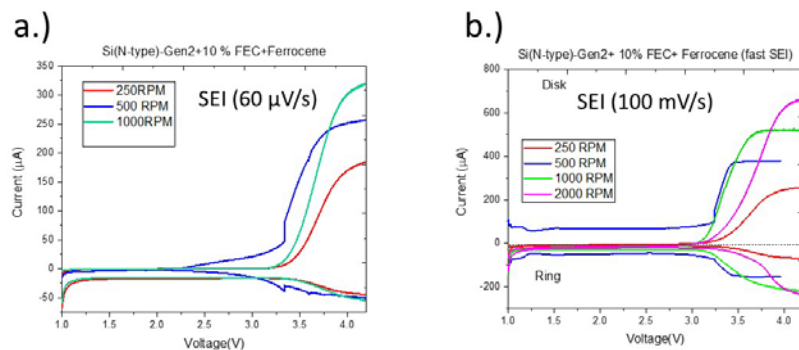


Figure 1.1.9.032.47. (a.) Si N-type disk electrode and Pt ring RRDE results shown for the oxidative side of the voltage window with 10 mM ferrocene in GEN2 + 10% FEC. This SEI was grown using 60 $\mu\text{V/s}$ rate, and (b.) 10 cycles at 100 mV/s SEI cycling formation.

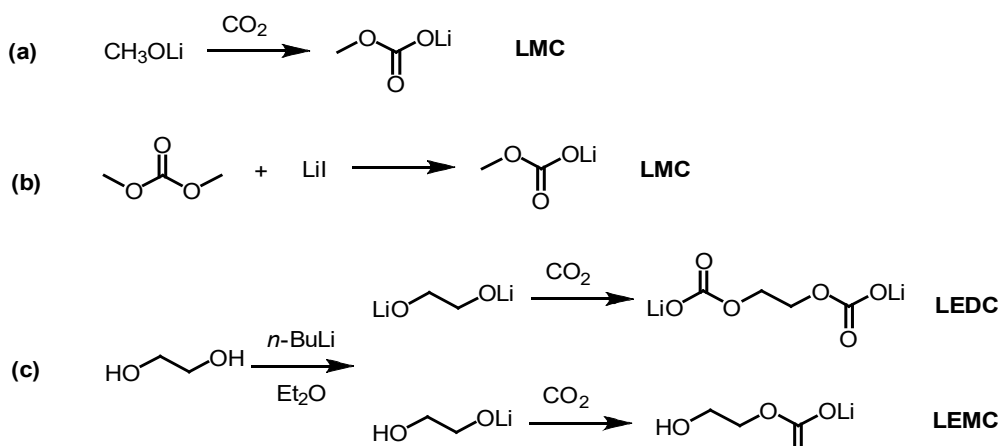


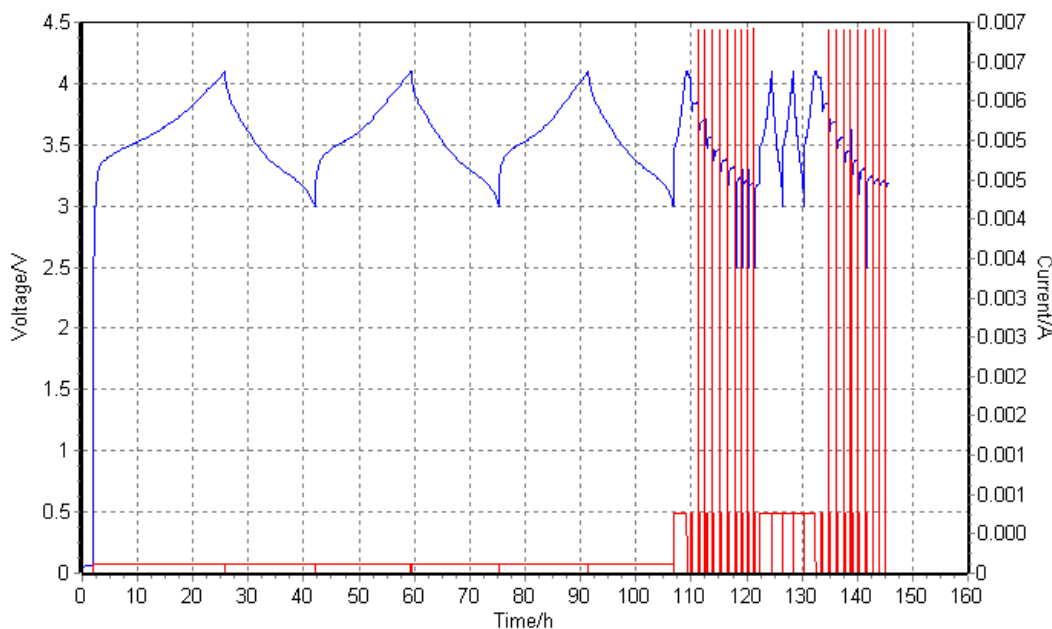
Figure 1.1.9.032.48. Synthetic scheme of PAA analogues with modified properties.

SEI Component Synthesis: In support of the soluble SEI species effort, the Lu Zhang group at Argonne synthesized several model compounds from the literature that have been reported to be significant components and / or stable phases in the silicon SEI. Identifying the components of the solid-electrolyte interphase (SEI) on silicon anodes is of crucial importance to enabling this promising chemistry. While many species have been synthesized and evaluated in graphite-based anodes, understanding silicon based SEI is still ongoing. This effort is to synthesize the known SEI components, such as lithium methyl carbonate (LMC), and lithium ethylene dicarbonate (LEDC), and to characterize their possible roles in the SEI formation process. As shown in **Figure 1.1.9.032.48**, LMC was synthesized in high yield and purified using a modified procedure according to literature. The attempt to synthesize LMC using lithium iodide was not working well due to the low yield and iodine contamination (**Figure 1.1.9.032.48b**). LEDC was synthesized using a reported procedure in moderate yield (**Figure 1.1.9.032.48c**). The characterization data matched those reported for this compound. Materials have been provided to interested DeepDive and SEISTA parties for analysis.

Cathode Interactions: The role of SEI speciation in a cell scan be affected by testing conditions. Previously we examined SEI components from thin film Si electrodes and via model electrode studies with no active phase. In comparison, the full Si-containing cell, with DeepDive cathodes, is the most complex test system as the number of species and the number of possible reactive sites is increased and this will affect the type and range

of organics found on the silicon electrode and the SEI. For these SEI component studies, two different cathodes were used, namely LiCoO_2 (LCO) and $\text{Li}(\text{Ni}_{0.5}\text{Mn}_{0.3}\text{Co}_{0.2})\text{O}_2$ (NMC532) in combination with a 80-wt% silicon cells containing Gen2+10wt% FEC. The LCO studies, although not a DeepDive baseline electrode, were used to evaluate the role of cathode dissolution and migration and Mn-containing cathode are known to have stability problems (cathode crosstalk). The catalytic properties of deposited manganese may alter the SEI speciation.

As alluded to above, the cycling regime used was very short, consisting of three C/20 cycles, a hybrid pulse-power characterization test (HPPC), two C/3 cycles and another HPPC test. This is shown in **Figure**



1.1.9.032.49

Figure 1.1.9.032.49 Voltage and current versus time, showing the testing regimen used for these short tests.

After cycling, the cells were taken apart and the electrolyte was recovered and characterized by HPLC/ESI-MS. These steps are shown schematically in **Figure 1.1.9.032.50** The CH_2Cl_2 layer was extracted and allowed to dry. The residue dissolved in acetonitrile and analyzed by HPLC.

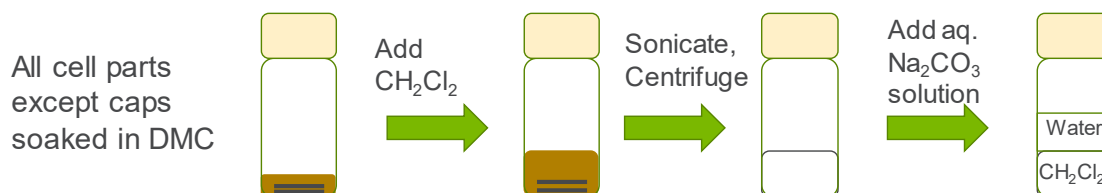


Figure 1.1.9.032.50. Schematic of electrolyte extraction steps.

The HPLC data indicated that there were five new compounds in the LCO case and four from NMC532. **Table 8** shows the retention times, molecular ion (m/e), number of carbons atoms and proposed empirical formulae of the species. When only one sample was present, an uncertainty of 10% was assumed in the number of carbons. Identification of the compounds is still in progress.

Table 8. Proposed compounds from HPLC data.

	Retention time, min	m/e, Da	No. of carbon atoms	Empirical formula
Si-LCO	3.4	408	18.4	$[C_{16}H_{32}O_{10}]Na^+$ (assuming $\pm 10\%$)
	5.5	215	6	$[C_5H_{11}O_7P]H^+$ (assuming $\pm 10\%$)
	6.6	243	6.5	?
	9.5	229	8.1	?
	13.9	90		$[EC]H^+$
	20	467	3?	?
Si-NMC	3.4	408	8.5 ± 0.6	?
	15.9	391	19.1 ± 0.5	?
	18.1	795	37.6 ± 1.6	$[C_{35}H_{70}O_{19}]H^+$
	20	467	21.5 ± 3.1	?

With these analysis and combined with previous reports on the role of temperature, the nature of the cathode material has a direct impact on changes in the organics found solubilized in the electrolyte.

LHCE Electrolytes: While variables such as SOC, cathode, and temperature stability can lead to SEI dissolution and premature cycling failure, alternative electrolytes that may offer different breakdown pathways and electrochemical window stability are not readily available. One that has been evaluated in the DeepDive is based on the concept of localized high concentration electrolytes (LHCEs) as the lack of free solvent partially eliminates a side-reaction degradation pathway noted in the Zintl section above. Previous reports have noted that with an alternative binder system (poly-imide), LHCEs can support cycling of silicon-based electrodes at room temperature, **Figure 1.1.9.032.51** shows the table of the LHCE diluent properties and the electrolyte compositions. The diluent 1,1,2,2-tetrafluoroethyl-2,2,3,3-tetrafluoropropyl ether (TTE) has a boiling point of 93.2°C and the 1H,1H,5H-Octafluoropentyl 1,1,2,2-Tetrafluoroethyl ether (OTE) has a boiling point of 133°C. The fundamental properties of the electrolytes were compared side-by-side.

The electrochemical performance was tested using standard DeepDive Si anodes in half-cell design (**Figure 1.1.9.032.52 a-c**) and full-cell (**Figure 1.1.9.032.52d-f**) with standard NMC532 cathodes from Argonne National Laboratory. Among all the LHCE electrolytes and baseline electrolyte, EL1 and EL3 with higher conductivity

delivered higher specific capacity in half-cell and better cycling stability. EL1 with DMC as bulk solvent and BTFE diluent showed the best overall performance with 91.6% first cycle Coulombic efficiency and excellent capacity retention over 50 cycles (**Figure 1.1.9.032.52 a-c**). In full-cell tests, cells using EL1 and EL3 showed similar specific capacity as those using baseline electrolyte and higher than those using EL2 and EL4. It confirms the trend in half cell tests. EL3 showed similar cycling performance to baseline electrolyte while EL1 showed the best cycling stability with almost no capacity fade over 50 cycles (**Figure 1.1.9.032.51 d-f**)

Longer chain length \longrightarrow

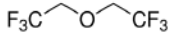
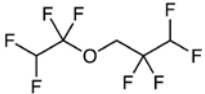
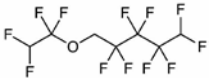
	BTFE (bis(2,2,2 trifluoroethyl)ether)	TTE (1,1,2,2 tetrafluoroethyl 2,2,3,3 tetrafluoropropyl ether)	OTE (1H,1H,5H Octafluoropentyl 1,1,2,2 Tetrafluoroethyl ether)
			
M.W.	182.06	232.07	332.09
B.P. (°C)	62-63	93.2	133
Density (g/ml)	1.404	1.5323	1.654
DMC solvent with different diluents			
EL1	LiFSI-DMC- BTFE (molar ratio = 0.51:1:2) + 1.0 wt% VC + 5 wt% FEC		
EL2	LiFSI-DMC- OTE (molar ratio = 0.51:1:2) + 1.0 wt% VC + 5 wt% FEC		
Ether solvent			
EL3	1 LiFSI-1.2DME-3TTE + 1.0 wt% VC + 5 wt% FEC		
Carbonate solvent			
EL4	1.8M LiFSI in EC-EMC (3:7 by wt.) -2TTE (molar ratio to EC/EMC)+1.0 wt% VC + 5 wt% FEC		

Figure 1.1.9.032.51 Molecular structure and properties of several diluents and the recipes of new LHCEs.

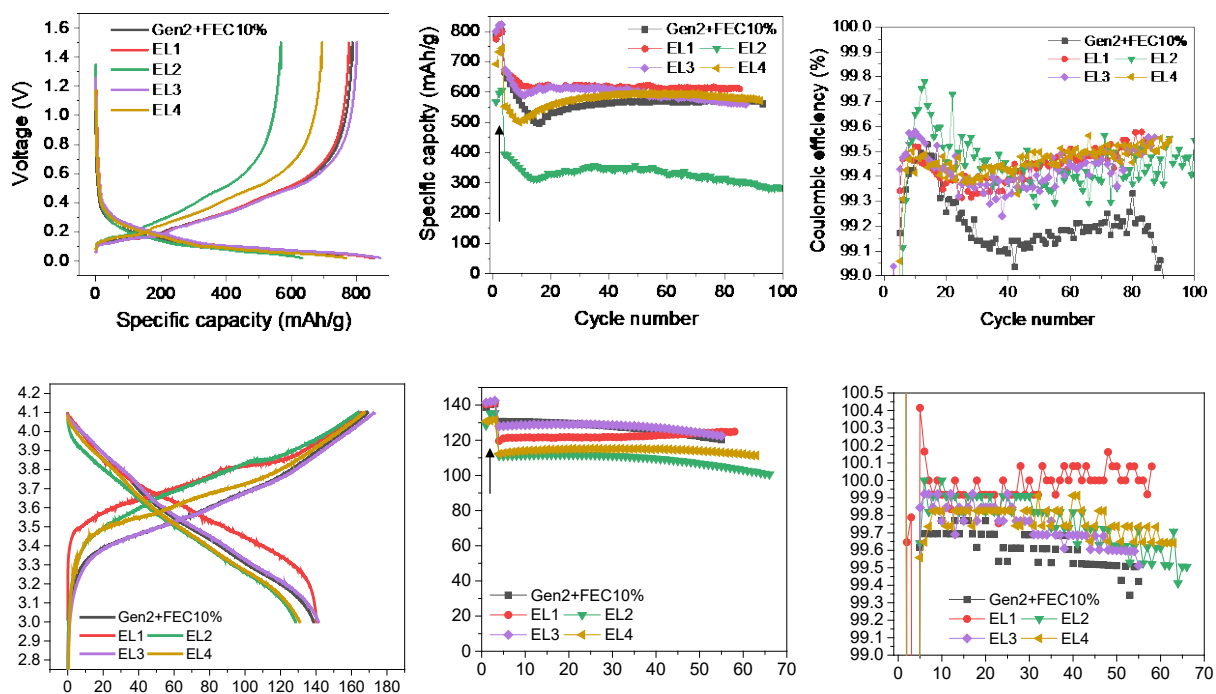


Figure 1.1.9.032.52. Charge-discharge curve, cycling stability, and Coulombic efficiency of DeepDive anodes in new LHCEs in half-cell (a-c) and full-cells (d-f) with NMC532 cathodes.

Conclusions: We have continued our investigation on SEI stability in full cell and extended our SEI/STC collaborations to include method development on identification of soluble species. Efforts using solvent polarity gradients have isolated various species as a function of electrochemical preparation and molecular properties. The method highlights the utility of this co-solvent approach. Studies in half cells and full cells using RRDE, HPLC, and other techniques have identified several phases that result from electrochemically mediated reactions between the silicon and the electrolyte. Collaborations with the synthetic organic synthesis group have been initiated to scale up and evaluate the properties of these identified phases as identified.

5. Key Publications

1. Rago, Nancy Dietz, Basco, John K, Anh Vu, Li, Jianlin, Hays, Kevin, Sheng, Yangping, Wood, DL Bloom, I “Effect of formation protocol: Cells containing Si-Graphite composite electrodes” *J. Power Sources* Vol **435** 126548 (2019) DOI: 10.1016/j.jpowsour.2019.04.076
2. Han, Binghong, Liao, Chen, Dogan, Fulya, Trask, Stephen E, Lapidus, SH, Vaughey, JT, Key, Baris “Using Mixed Salt Electrolytes to Stabilize Silicon Anodes for Lithium-Ion Batteries via in Situ Formation of Li-M-Si Ternaries (M = Mg, Zn, Al, Ca)” *ACS Appl Materials and Interfaces* **11**, 29780-29790 (2019) DOI: 10.1021/acsami.9b07270
3. Nanda, Jagjit; Yang, Guang, Hou; TZ; Voylov, DN; Li, X; Ruther, RE; Naguib, M; Persson, K; Veith,; Sokolov, AP “Unraveling the Nanoscale Heterogeneity of Solid Electrolyte Interphase Using Tip-Enhanced Raman Spectroscopy” *Joule*, **3**, 2001-2019 (2019) DOI: 10.1016/j.joule.2019.05.026
4. Yoon, Taeho; Xiao, Chuanxiao; Liu, Jun; Wang, Yikai; Son, Seoungbum; Burrell, A; Ban, CM “Electrochemically induced fractures in-crystalline silicon anodes” *J. Power Sources*, **425** 44-49 (2019) DOI: 10.1016/j.jpowsour.2019.03.105
5. Xu, Yun; Wood, Kevin; Coyle, J; Engtrakul, C; Teeter, G; Stoldt, C; Burrell, A; Zakutayev, A “Chemistry of Electrolyte Reduction on Lithium Silicide” *J. Phys Chem C.*, **123** 13219-13224 (2019) DOI: 10.1021/acs.jpcc.9b02611
6. K.P.C. Yao, J.S. Okasinski, K. Kalaga, J.D. Almer, D.P. Abraham, “Operando Quantification of (De)Lithiation Behavior of Silicon-Graphite Blended Electrodes for Lithium-Ion Batteries”, *Adv. Energy Mater.* **9** 1803380 (2019).
7. K. Kalaga, M.-T. Rodrigues, S.E. Trask, I.A. Shkrob, D.P. Abraham, “Calendar-life versus Cycle-life aging of Lithium-ion Cells with Silicon-Graphite Composite Electrodes”, *Electrochimica Acta* **280** 221 (2018).
8. Yao, K.; Ling, M.; Liu, G.; Tong, W., Chemical Reduction Synthesis and Electrochemistry of Si-Sn Nanocomposites as High-Capacity Anodes for Li-Ion Batteries. *J. Phys. Chem. Lett.* (2018), **9** (17), 5130-5134.
9. Hannah R. Morin, María José Piernas Muñoz, Stephen E. Trask, Alison R. Dunlop, Ira Bloom “Effect of Cathode on Changes in the Electrolyte: A First Step to Understand ‘Cross-talk’ in Si-based Lithium-ion Cells” *J. Power Sources*, submitted, (2019).
10. H. Jia, L. Zou, P. Gao, Cao Xia, W. Zhao, Yang He, Mark H. Engelhard, S. D. Burton, Hui Wang, X. Ren, Q. Li, Ran Yi, Xin Zhang, C. Wang, Z. Xu, X. Li, J. Zhang, Wu Xu, “High performance silicon anodes enabled by nonflammable localized high concentration electrolytes,” *Advanced Energy Materials*, (2019) <https://doi.org/10.1002/aenm.201900784>
11. Hu, Bin; Jiang, Sisi; Shkrob, Ilya A.; Zhang, Jingling; Trask, Stephen E; Polzin, Bryant; Jansen, Andrew; Chen, W; Liao, C; Zhang, ZC ; Zhang, L. “Understanding of pre-lithiation of poly(acrylic acid) binder: Striking the balances between the cycling performance and slurry stability for silicon-graphite composite electrodes in Li-ion batteries” *J. Power Sources* **416** p 125-131 (2019) DOI: 10.1016/j.jpowsour.2019.01.068
12. Jiang, SS; Hu, Bin; Sahore, Ritu; Zhang, Linghong; Liu, HH; Zhang, L; Lu, WQ; Zhao, B; Zhang, ZC “Surface-Functionalized Silicon Nanoparticles as Anode Material for Lithium-Ion Battery” *ACS Appl Materials and Interfaces* **10** 44924-44931 (2018) DOI: 10.1021/acsami.8b17729
13. Chen, H; Ling, M; Hencz, L; Ling, HY; Li, GR; Lin, Z; Liu, G; Zhang, SQ “Exploring Chemical, Mechanical, and Electrical Functionalities of Binders for Advanced Energy-Storage Devices” *Chem Rev* **118**, 8936-8982 (2018) DOI: 10.1021/acs.chemrev.8b00241
14. Han, BH; Piernas-Munoz, ZJ; Dogan, F; Kubal, J; Trask, SE; Bloom, ID; Vaughey, J.; Key, B “Probing the Reaction between PVDF and LiPAA vs Li₇Si₃: Investigation of Binder Stability for Si Anodes” *J. Electrochem Soc.*, **166**, A2396-A2402 (2019) DOI: 10.1149/2.0241912jes

6. References

- M.N. Obrovac and V.L. Chevrier “Alloy Negative Electrodes for Li-Ion Batteries”, *Chem. Rev.* 2014, 114, 11444-11503.
- P. Nelson, D. Dees, K. Gallagher, S. Ahmed “*Modeling the Performance and Cost of Lithium-Ion Batteries for Electric-Drive Vehicles*” Second Edition, Argonne National Laboratory Report, ANL-12/55.
- Wu H.; Cui, Y. *Nano Today* **2012**, 7 (5), 414-429.
- Hu B.; Shkrob I. A.; Zhang S.; Zhang L.; Zhang J.; Li Y.; Liao C.; Zhang Z.; Lu W.; Zhang L. *J. Power Sources* **2019**, 416, 125-131.
- Erogbogbo F.; Lin T.; Tucciarone P. M.; LaJoie K. M.; Lai L.; Patki G. D.; Prasad P. N.; Swihart M. T. *Nano Lett.* **2013**, 13(2), 451-456.
- G. V. Zhuang, H. Yang, P. N. Ross, Jr., K. Xu, and T. R. Jow, *Electrochem. Solid-State Lett.* **2006**, 9, A64-A68.
- H. Liu, X. Wang, H. Zhou, H. Lim, X. Xing, Q. Yan, Y. S. Meng, and P. Liu, *ACS Appl. Energy Mater.* **2018**, 1, 1864-1869.
- G. V. Zhuang, K. Xu, H. Yang, T. R. Jow, and P. N. Ross, Jr., *J. Phys. Chem. B* **2005**, 109, 17567-17573.
- L. Wang, A. Menakath, F. Han, Y. Wang, P. Y. Zavalij, K. J. Gaskell, O. Borodin, D. Luga, S. P. Brown, C. Wang, K. Xu, and B. W. Eichhorn, *Nat. Chem.* **2019**, 11, 789-796.
- Choi, S., et al., *Highly elastic binders integrating polyrotaxanes for silicon microparticle anodes in lithium ion batteries*. *Science*, 2017. **357**(6348): p. 279-283.
- Munaoka, T., et al., *Ionicallly Conductive Self-Healing Binder for Low Cost Si Microparticles Anodes in Li-Ion Batteries*. *Advanced Energy Materials*, 2018. **8**(14): p. 1703138.
- Yoon, T., "Electrochemically induced fractures in crystalline silicon anodes" *Journal of Power Sources*, 2019. **425**: p. 44-49.
- Meyers, M.A. and K.K. Chawla, "*Mechanical Behavior of Materials*", Upper Saddle River, New Jersey: Prentice-Hall, Inc. (1999)
- Sarkar, A., P. Shrotriya, and A. Chandra "Fracture Modeling of Lithium-Silicon Battery Based on Variable Elastic Moduli" *Journal of The Electrochemical Society*, 2017. **164**(11): p. E3606-E3612.
- Wei, L. "Poly (acrylic acid sodium) grafted carboxymethyl cellulose as a high performance polymer binder for silicon anode in lithium ion batteries". *Scientific Reports*, 2016. **6**: p. 19583.
- Bosco, N., J. Tracy, and R. Dauskardt, "Environmental Influence on Module Delamination Rate" *IEEE Journal of Photovoltaics*, 2019. **9**, p. 469-475.
- Ahn, H.-J.; Kim, Y.-S.; Park, K.-W.; Seong, T.-Y. “Use of Sn-Si nanocomposite electrodes for Li rechargeable batteries” *Chemical Communications* 2005, (1), 43-45.
- Hatchard, T.; Dahn, J. Study of the electrochemical performance of sputtered Si_{1-x}Sn_x films. *J. Electrochem. Soc.* **2004**, 151 (10), A1628–A1635.
- Xiao, X.; Wang, J. S.; Liu, P.; Sachdev, A. K.; Verbrugge, M. W.; Haddad, D.; Balogh, M. P. Phase-separated silicon–tin nanocomposites for high capacity negative electrodes in lithium ion batteries. *J. Power Sources* **2012**, 214, 258–265.

- Xu, J.; Ling, M.; Terborg, L.; Zhao, H.; Qiu, F.; Urban, J. J.; Kostecki, R.; Liu, G.; Tong, W. Facile synthesis and electrochemistry of Si-Sn-C nanocomposites for high-energy Li-ion batteries. *J. Electrochem. Soc.* **2017**, *164* (7), A1378–A1383.
- Yao, K.; Ling, M.; Liu, G.; Tong, W. Chemical reduction synthesis and electrochemistry of Si-Sn nanocomposites as high-capacity anodes for Li-Ion batteries. *J. Phys. Chem. Lett.* **2018**, *9* (17), 5130–5134.
- M. -T. F. Rodrigues, S. E. Trask, I. A. Shkrob, D. P. Abraham, “Quantifying gas generation from slurries used in fabrication of Si-containing electrodes for lithium-ion cells”, *J. Power Sources* **395**, 289 (2018).
- Han, Binghong, Liao, Chen, Dogan, Fulya, Trask, Stephen E, Lapidus, SH, Vaughey, JT, Key, Baris “Using Mixed Salt Electrolytes to Stabilize Silicon Anodes for Lithium-Ion Batteries via in Situ Formation of Li-M-Si Ternaries (M = Mg, Zn, Al, Ca)” *ACS Appl Materials and Interfaces* **11**, 29780-29790 (2019) DOI: 10.1021/acsami.9b07270
- Dogan, F.; Croy, J. R.; Balasubramanian, M.; Slater, M. D.; Iddir, H.; Johnson, C. S.; Vaughey, J. T.; Key, B., Solid State NMR Studies of Li₂MnO₃ and Li-Rich Cathode Materials: Proton Insertion, Local Structure, and Voltage Fade. *Journal of the Electrochemical Society* **2015**, *162* (1), A235-A243.
- Dose, W. M.; Maroni, V. A.; Piernas-Muñoz, M. J.; Trask, S. E.; Bloom, I.; Johnson, C. S., Assessment of Li-Inventory in Cycled Si-Graphite Anodes Using LiFePO₄ as a Diagnostic Cathode. **2018**, *165* (10), A2389-A2396.
- Pan, C.; Nuzzo, R. G.; Gewirth, A. A., ZnAl_xCo_{2-x}O₄ Spinels as Cathode Materials for Non-Aqueous Zn Batteries with an Open Circuit Voltage of ≤2 V. *Chemistry of Materials* **2017**, *29* (21), 9351-9359.
- “High performance silicon anodes enabled by nonflammable localized high concentration electrolytes,” Haiping Jia, Lianfeng Zou, Peiyuan Gao, Cao Xia, Wengao Zhao, Yang He, Mark H. Engelhard, Sarah D. Burton, Hui Wang, Xiaodi Ren, Qiuyan Li, Ran Yi, Xin Zhang, Chongmin Wang, Zhijie Xu, Xiaolin Li, Jiguang Zhang, Wu Xu, published online in *Advanced Energy Materials*, <https://doi.org/10.1002/aenm.201900784>